Roles of Dynamic and Thermodynamic Processes in Regulating the Decay Paces of El Niño Events

CHUNG-WEI LEE,[a] CHUNG-HSIUNG SUI,[a] AND TIM LI[b,c]

[a] *Department of Atmospheric Sciences, National Taiwan University, Taipei, Taiwan*
[b] *International Pacific Research Center and Department of Atmospheric Sciences, School of Ocean and Earth Science and Technology, University of Hawai'i at Mānoa, Honolulu, Hawaii*
[c] *Key Laboratory of Meteorological Disaster, Ministry of Education (KLME), Nanjing University of Information Science and Technology, Nanjing, China*

ABSTRACT: Most El Niño events decay after a peak in boreal winter, but some persist and strengthen again in the following year. Several mechanisms for regulating its decay pace have been proposed; however, their relative contributions have not been thoroughly examined yet. By analyzing the fast-decaying and persistent types of the events in a 1200-yr coupled simulation, we quantify the key dynamic and thermodynamic processes in the decaying spring that are critical to determining the decay pace of El Niño. The zonal advection due to upwelling Kelvin wave accounts for twice as much the cooling difference as evaporation or meridional advection does. The upwelling Kelvin wave is much stronger in the fast-decaying events than the others, and its strength is equally attributed to the reflected equatorial Rossby wave and the equatorial easterly wind forcing over the western Pacific in the preceding 2–3 months. Relative to the fast-decaying events, the evaporative cooling is weaker but the meridional warm advection is stronger in the persistent events. The former is due to more meridionally asymmetric wind and sea surface temperature anomalies (SSTA) signaling positive Pacific meridional mode. The latter results from the advection of equatorial warm SSTA by climatological divergent flow, and the warmer SSTA persists from the mature stage subject to weaker cloud-radiative cooling in response to the central-Pacific-type SSTA distribution in the persistent events relative to the fast-decaying events. Our result consolidates the existing knowledge and provides a more comprehensive and physical pathway for the causality of El Niño's diverse duration.

KEYWORDS: Atmosphere–ocean interaction; El Nino; Interannual variability

1. Introduction

El Niño–Southern Oscillation (ENSO) is an atmosphere–ocean coupled phenomenon over the tropical Pacific with its warm (El Niño) and cold (La Niña) phases reoccurring every few years, and it has a profound impact on the global climate (e.g., Rasmusson and Carpenter 1982; Ropelewski and Halpert 1987; Trenberth et al. 1998; Li and Hsu 2017). ENSO's growth is largely modulated by the seasonal cycle (Jin et al. 1994; Tziperman et al. 1994; Li 1997; Tziperman et al. 1997; Stein et al. 2010); an El Niño event usually develops in boreal summer and fall with positive Bjerknes feedback (Bjerknes 1969), peaks in winter, and decays in spring.

From a linear perspective of the delayed oscillator (e.g., Suarez and Schopf 1988; Battisti and Hirst 1989) and the recharge–discharge oscillator (Jin 1997; Li 1997; Meinen and McPhaden 2000), El Niño grows with positive Bjerknes feedback (Bjerknes 1969), while the key to its phase transition lies in the delayed negative feedbacks from oceanic response to the anomalous winds in the development stage. The delayed oscillator theory emphasizes the role of oceanic Rossby wave that is reflected at the western boundary to the equator as Kelvin waves to reverse ENSO's phase, while the recharge–discharge oscillator highlights the variation of basin-integrated warm water volume (WWV) resulting from meridional

Sverdrup transport. Some other processes can also facilitate the abrupt termination of El Niño events. For instance, Weisberg and Wang (1997) and Wang et al. (1999) suggested easterly wind anomalies on the equatorial flank of an El Niño–induced anomalous anticyclone over the western North Pacific (WNPAC; e.g., Wang et al. 2000; Wang and Zhang 2002; Wu et al. 2017a,b) can induce upwelling Kelvin waves that propagate to the equatorial eastern Pacific and end the positive feedback. H.-C. Chen et al. (2016) demonstrated the reversal of zonal transport due to a change of meridional concavity of the thermocline structure associated with downwelling Kelvin waves reflected at the eastern boundary can sharply terminate the warm event. Some other studies (Harrison 1987; Harrison and Vecchi 1999; McGregor et al. 2012, 2013) found that tropical zonal wind anomalies become asymmetric about the equator in the El Niño mature phase, and that the southward shift of westerly wind anomalies is essential in strong El Niño's drastic turnabout by causing oceanic dynamic response. This interaction involves the establishment of South Pacific convergence zone (SPCZ) in winter, so its spectrum falls in a near-annual period as a combination mode (harmonic) of the interannual variability (ENSO) and annual cycle (e.g., Stuecker et al. 2013). The combination mode describes not only ENSO's fast termination and its seasonal phase-locking behavior, but also other climate impacts such as WNPAC (Stuecker et al. 2015).

In addition to dynamic processes, Dommenget and Yu (2016) showed that the negative sea surface temperature

Corresponding author: Chung-Hsiung Sui, sui@as.ntu.edu.tw

(SST)–shortwave radiation–cloud feedback acts to dampen ENSO in the beginning of the year when springtime climatological SST over the equatorial eastern Pacific is the warmest and more favorable for deep convection to develop. By diagnosing the oceanic mixed layer budget with observational data, M. Chen et al. (2016) demonstrated that both the dynamic (3D temperature advection) and thermodynamic (e.g., shortwave and latent heat flux) processes are crucial in causing El Niño's more rapid termination than La Niña's.

Most observed El Niño events rapidly decay to the neutral or opposite phase after the mature stage, but still about a third of events have an extended warm period into the second winter (Wu 2018; Wu et al. 2019; Lee et al. 2020), such as 2014–16 (e.g., Menkes et al. 2014; McPhaden 2015; Min et al. 2015 Maeda et al. 2016; Levine and McPhaden 2016; Chen et al. 2017). Through analysis of observation episodes, Lee et al. (2020) documented that the onsets of SST and equatorial westerly wind anomalies in persistent El Niño events are later than those of the single-year event composite by about a season. Analyzing both model and observation data, Wu et al. (2019) showed that there exists an overall linear relationship between El Niño's onset timing and duration despite a large variability. Wu et al. (2019) proposed that the delayed onset leads to a later arrival of the negative oceanic feedback (delayed oscillator), while Lee et al. (2020) showed that in association with the later onset, the discharge of warm water volume (WWV) by equatorial cyclonic wind anomalies in the developing and mature stages was insufficient to overturn the warm condition in the equatorial central-eastern Pacific. As for the reason for the later onset, Lee et al. (2020) found that 4 of 5 observed prolonged El Niños were accompanied by a strengthened cross-hemisphere SST gradient and cross-equatorial southerly anomalies over the tropical eastern Pacific during development seasons, which might prohibit the equatorward migration of the intertropical convergence zone (ITCZ) and disrupt the positive Bjerknes feedback (Bjerknes 1969) in the zonal direction and cause slower growth.

Besides the coupled processes mentioned above, a rapid or slow decay of ENSO involves interaction of the equatorial Pacific with the Indian Ocean. Previous studies have shown the abrupt wind reversal over the equatorial western Pacific in El Niño's mature stage associated with the demise of positive IOD (pIOD) in the preceding autumn can accelerate El Niño's decay (Kug and Kang 2006; Izumo et al. 2010, 2016). Wu et al. (2019) and Kim and Yu (2020) also found distinctive differences in the equatorial zonal wind anomalies over the equatorial western Pacific during the decaying stage between single-year and persistent El Niño events. Wu et al. (2019) attributed the different equatorial western Pacific zonal winds to the interbasin SST gradient, which arises from stronger or weaker Indian/Atlantic Ocean responses to earlier or later El Niño's onsets, whereas Kim and Yu (2021) found El Niño events with a more eastern onset location of SST are more capable of activating Indo-Pacific interactions via anomalous Walker circulation.

Extratropical variability such as the Pacific meridional mode (PMM; Vimont et al. 2001, 2003a,b; Chiang and Vimont 2004; Chang et al. 2007; Zhang et al. 2009; Alexander et al. 2010; Yu et al. 2010; Anderson et al. 2013; Larson and Kirtman 2013; Di Lorenzo et al. 2015) in the decaying stage can affect El Niño's evolution as well. Wu et al. (2019) noted that the pattern of extratropical wind difference between single-year and persistent El Niño resembles the North Pacific Oscillation (NPO), whereas Kim and Yu (2020) showed that the negative phase of the NPO occurs more frequently in the mature winter of prolonged El Niño events. Ding et al. (2022) demonstrated that the CP-type El Niño and NPO can feed back on each other and result in multiyear El Niño.

Although several mechanisms have been proposed for ENSO decaying as reviewed above, we still do not have convincing enough evidence to reach conclusive understanding due to limited events and large diversities of ENSO observation. In this study, we look at 244 El Niño events from a 1200-yr preindustrial control (piControl) simulation of National Center for Atmospheric Research (NCAR) Community Earth System Model, version 2 (CESM2; Danabasoglu et al. 2020), from phase 6 of the Coupled Model Intercomparison Project (CMIP6; Eyring et al. 2016) to investigate mechanisms for fast-decaying, slow-decaying, and persistent El Niño groups. The goal of this study is to perform an in-depth comparison of the processes between different decay types of El Niño by quantifying the relative roles of these processes and explaining the corresponding mechanisms in regulating the decay paces of El Niño.

This paper is organized as follows. Section 2 documents data and methods, section 3 shows the overall evolutions of El Niño of different duration types, and in section 4 we analyze the mixed layer heat budget. After sections 3 and 4 reveal the critical role of upwelling Kelvin waves in the decaying stage, then section 5 explores the factors controlling the strength of upwelling Kelvin waves. Section 6 is a summary, and section 7 provides discussion.

2. Data and methods

The 1200-yr piControl simulation of NCAR CESM2 (Danabasoglu et al. 2020) from CMIP6 is used in this study for a large sample size of El Niño events. CESM2 is able to simulate the mean climate state over the tropical Pacific, ENSO's spatial and temporal features, and the dynamics of recharge–discharge oscillator reasonably well, despite a bias of larger equatorial Pacific SST variability (Capotondi et al. 2020).

El Niño events are identified by the 3-month running mean Niño-3.4 index, which is SST anomalies averaged over 170°–120°W, 5°S–5°N. A warm period is defined when the index is continuously positive, and an El Niño peak is defined at local maximums when the index is above 0.7 standard deviations (~0.78°C in CESM2) for more than 5 consecutive months. This criterion corresponds to 0.63°C in 1981–2010 Extended Reconstructed SST version 5 (ERSSTv5; Huang et al. 2017). Within one warm period, if there are two adjacent peaks at an interval equal to or less than 12 months, they are considered to belong to the same "persistent" event. The rest of them are "fast-decaying" or "slow-decaying" types. Those whose index turns negative before the summer past the peak, June–August[1] (JJA[1]), are categorized as the fast-decaying

group; those whose index remains above zero until JJA[1] are defined as the slow-decaying events. Additionally, 10 events with more than two neighboring peaks in a warm period are discarded in this study. There are 244 El Niño events in the 1200-yr simulation, and they consist of 107 (44%) fast-decaying, 89 (36%) slow-decaying, and 48 (20%) persistent events.

In comparison, Wu et al. (2019) selected 0.75 and 0.5 standard deviations for the first and second peaks, respectively, in any month from October to the following February, while Kim and Yu (2020) only considered the weak events with the first peak between 0.5 and 1.0 standard deviation in December. Our detection method is seasonally independent and does not assume whether the first peak is strong or weak, but the threshold is higher.

The mixed layer heat budgets are analyzed in section 4 to quantify the relative importance of each process. The budget terms are decomposed as (Hong et al. 2008; Su et al. 2010; M. Chen et al. 2016; Chen et al. 2017)

$$
\frac{\partial T'}{\partial t} = -u'\frac{\partial \overline{T}}{\partial x} - v'\frac{\partial \overline{T}}{\partial y} - w'\frac{\partial \overline{T}}{\partial z} - \overline{u}\frac{\partial T'}{\partial x}
$$
$$
- \overline{v}\frac{\partial T'}{\partial y} - \overline{w}\frac{\partial T'}{\partial z} - u'\frac{\partial T'}{\partial x} - v'\frac{\partial T'}{\partial y} - w'\frac{\partial T'}{\partial z}
$$
$$
+ \frac{\mathrm{LW'} + \mathrm{SW'} + \mathrm{LH'} + \mathrm{SH'}}{\rho_{\mathrm{sea}} C_p H}. \tag{1}
$$

The overbar denotes climatology, and the prime denotes anomaly; T is the oceanic temperature; (u, v, w) represents three-dimensional currents; LW, SW, LH, and SH represent surface longwave, shortwave, latent heat, and sensible heat fluxes, respectively; and constants ρ_{sea} and C_p are density (10^3 kg m^{-3}) and specific heat (4000 J kg^{-1} K^{-1}) of seawater, respectively. The mixed layer depth H is defined as the depth where temperature is 0.5°C cooler than the surface, which varies with time and space, and is between 25 and 75 m over the Niño-3.4 region. The budget terms are integrated from surface to the mixed layer depth and averaged over the Niño-3.4 region.

To investigate the mechanisms associated with the zonal component of advective cooling/warming, the geostrophic (u_g) and Ekman (u_e) components of zonal currents are estimated as (Su et al. 2010)

$$
u_g = -\frac{g'}{\beta}\frac{\partial^2 h}{\partial y^2} \quad \text{and} \quad u_e = \frac{1}{\rho_{\mathrm{sea}} H_1}\frac{r_s \tau^x + \beta y \tau^y}{r_s^2 + (\beta y)^2}. \tag{2}
$$

In Eq. (2), (τ^x, τ^y) are two-dimensional surface wind stresses, and h is thermocline depth. The constant g' is the reduced gravity acceleration (0.026 m s^{-2}), β is the Rossby parameter (2.279×10^{-11} m^{-1} s^{-1}), ρ_{sea} is seawater density (10^3 kg m^{-3}), H_1 is the Ekman layer depth (50 m), and r_s is the dissipation rate (0.5 day^{-1}).

The contribution of latent heat is also estimated by bulk formula, and is decomposed into specific humidity gradient term, wind speed term, and nonlinear term as

$$
\mathrm{LH'} \approx [-\rho_0 C_d U(Q_s - Q)]'
$$
$$
= -\rho_0 C_d \overline{U}(Q_s - Q)' - \rho_0 C_d U'\overline{(Q_s - Q)}
$$
$$
- \rho_0 C_d U'(Q_s - Q)'. \tag{3}
$$

The terms U, Q, and Q_s represent surface wind speed (m s^{-1}), specific humidity (kg kg^{-1}), and saturation specific humidity (kg kg^{-1}), respectively. The constant ρ_0 is air density (1 kg m^{-3}), C_d is the drag coefficient (1.3×10^{-3}), and L_v is the specific latent heat capacity (2.5×10^6 J kg^{-1}).

Following Boulanger and Menkes (1995), the oceanic equatorial waves are spatially filtered by projecting the anomalies on the theoretical meridional structure derived from the shallow water system on a beta plane. These theoretical structures are linear combinations of normalized Hermite polynomials ψ_n. For a Kelvin wave, its structure of zonal velocity and geopotential height is $R_0^{u,h}$:

$$
R_0^{u,h} = \frac{1}{\sqrt{2}}\psi_0(y), \tag{4.1}
$$

For a Rossby wave, we only consider the gravest mode, and its zonal velocity and geopotential height structures are R_1^u and R_1^h, respectively:

$$
R_1^u = \frac{1}{\sqrt{3}}\left[\frac{1}{\sqrt{2}}\psi_2(y) - \psi_0(y)\right] \quad \text{and} \tag{4.2}
$$

$$
R_1^h = \frac{1}{\sqrt{3}}\left[\frac{1}{\sqrt{2}}\psi_2(y) + \psi_0(y)\right]. \tag{4.3}
$$

The gravity wave speed (C_0) is 3.0 m s^{-1}, and the projection is calculated from 15°S to 15°N.

Anomalies are calculated as the deviation from 1200-yr mean climatology, and the linear trend over the whole period is removed. The 20°C-isotherm depth (D20) is taken as the proxy for thermocline depth. The anomalies and heat budget are calculated on the model's native grid and interpolated to a 1° × 1° longitude–latitude grid for plotting. The year before the winter of El Niño's first peak (i.e., developing year) is denoted by 0, as the superscript in year[0]. Bootstrap resampling with a size of 10 000 is used to test whether the difference between each type is statistically significant and to calculate the confidence interval.

3. Overall evolutions of El Niño of different duration types

The Niño-3.4 SST anomalies in all of the three groups of El Niño grow in summer and autumn (June[0]–November[0]) and reach their maximums in boreal winter (December[0]–January[1]; Fig. 1a); although they have distinct event durations, their growth rates appear to be modulated by the seasonal cycle. By definition, the fast-decaying group rapidly diminishes before the ensuing summer (JJA[1]), the slow-decaying group gradually weakens to a neutral condition, and the persistent group persists into the next winter (December[1]–February[2]; D[1]JF[2]). The
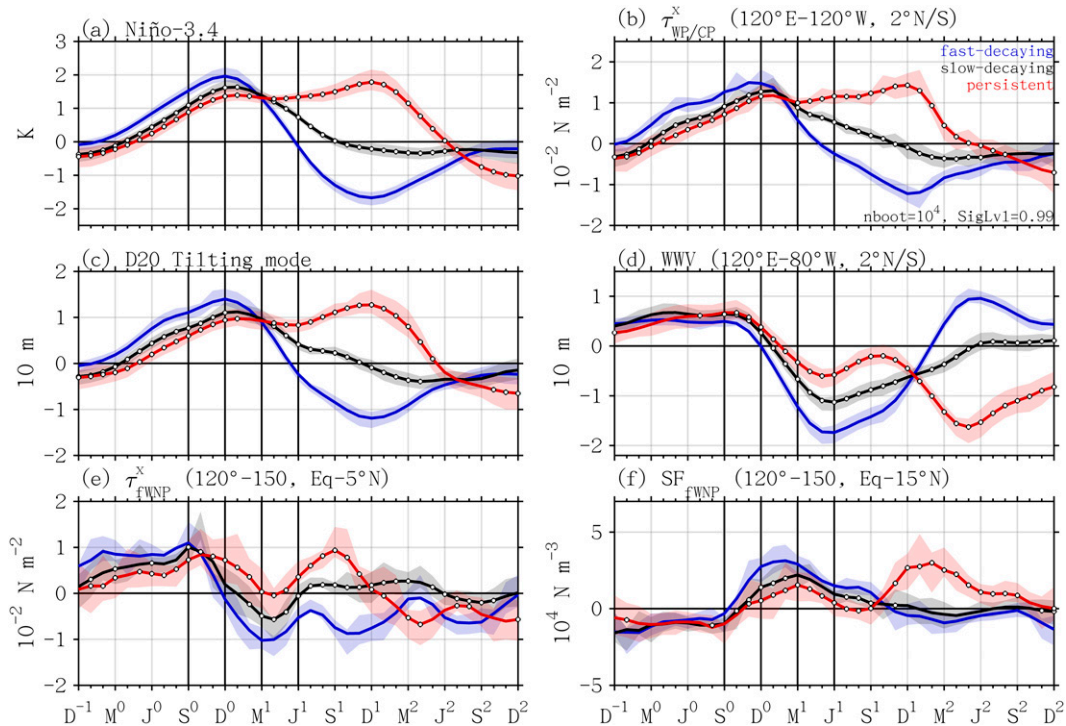
FIG. 1. The composite evolution of fast-decaying (blue), slow-decaying (black), and persistent (red) El Niño events in (a) the Niño-3.4 index, (b) the surface zonal wind stress anomalies averaged over the equatorial western/central Pacific (120°E–120°W, 2°N/S), (c) the tilting mode of thermocline defined as the D20 anomalies averaged over the equatorial eastern Pacific (155°–80°W, 2°N/S) minus that averaged over the equatorial western Pacific (120°E–155°W, 2°N/S), (d) the warm water volume calculated as the D20 anomalies averaged over the equatorial Pacific basin (120°E–80°W, 2°N/S), (e) the surface zonal wind stress anomalies averaged over the equatorial far western North Pacific (120°–150°E, 0°–5°N), and (f) the strength of WNPAC defined as streamfunction anomalies averaged over the far western North Pacific (120°–150°E, 0°–15°N). The color shading shows the 0.99 confidence interval in each type. The dots denote where the difference from the fast-decaying group is significant at 0.99 confidence level. The vertical thick lines denote September[0], December[0], March[1], and June[1].

persistent group is still phase-locked to the seasonal cycle in year 1 and 2 as it slightly weakens in March–May[1] (MAM[1]), reintensifies in the following autumn [September–November[1] (SON[1])], reaches another peak in December[1], and decays in the succeeding spring (MAM[2]). Also, the evolutions of Niño-3.4 SST (Fig. 1a), equatorial westerly (Fig. 1b), and thermocline tilting (Fig. 1c) on the basin scale are nearly in phase with one another regardless of the duration types, indicating the fundamental role of Bjerknes feedback (Bjerknes 1969) for the ENSO dynamics. Here, we define SON[0], D[0]JF[0], and MAM[1] as the growth, mature, and decay stages, and they are demarcated by the thick vertical lines in Fig. 1.

The WWV index indicates that the equatorial Pacific is in the recharged state during the development year in all groups (Fig. 1d). However, the preconditioning effect of the WWV for different types is indistinguishable, as their differences are not significant before June[0] (except for December[0]). Nevertheless, after September[0], it becomes clear that the discharge is faster and earlier in the fast-decaying group than the slow-decaying and persistent ones.

The significant differences in Niño-3.4 indices occur not only after the mature stage but also during the growth stage

(Fig. 1a). In year[0], the fast-decaying group is stronger than the others, and its onset is relatively earlier by 3–4 months, which is consistent with Wu et al. (2019) and Lee et al. (2020). It induces stronger equatorial Pacific westerly wind anomalies as it develops earlier (Fig. 1b), and it is accompanied by a pIOD response over the Indian Ocean in the growth stage (Fig. 2a), which further enhances the equatorial Pacific westerly wind anomalies by strengthening the anomalous atmospheric cooling over the "Maritime Continent" and the heating over the central Pacific (Fig. 2j). In response to the cyclonic wind stress curls associated with the equatorial Pacific westerly wind anomalies, equatorial upwelling Rossby waves are excited and the thermocline shoals in the equatorial western Pacific (Fig. 2j). The weaker Pacific cold tongue induces the anomalous equatorward flow (Fig. 2a) and the southward shift of the Pacific ITCZ as shown by negative D20 anomalies along ~6°N and the associated rainfall anomalies (Fig. 2j). Also, the oceanic heat content begins to decrease over the equatorial western Pacific. For the persistent group, in contrast, both El Niño and pIOD SST anomalies are less prominent in the growth stage (Figs. 2b,c), the suppressed precipitation over the Maritime Continent is less organized,
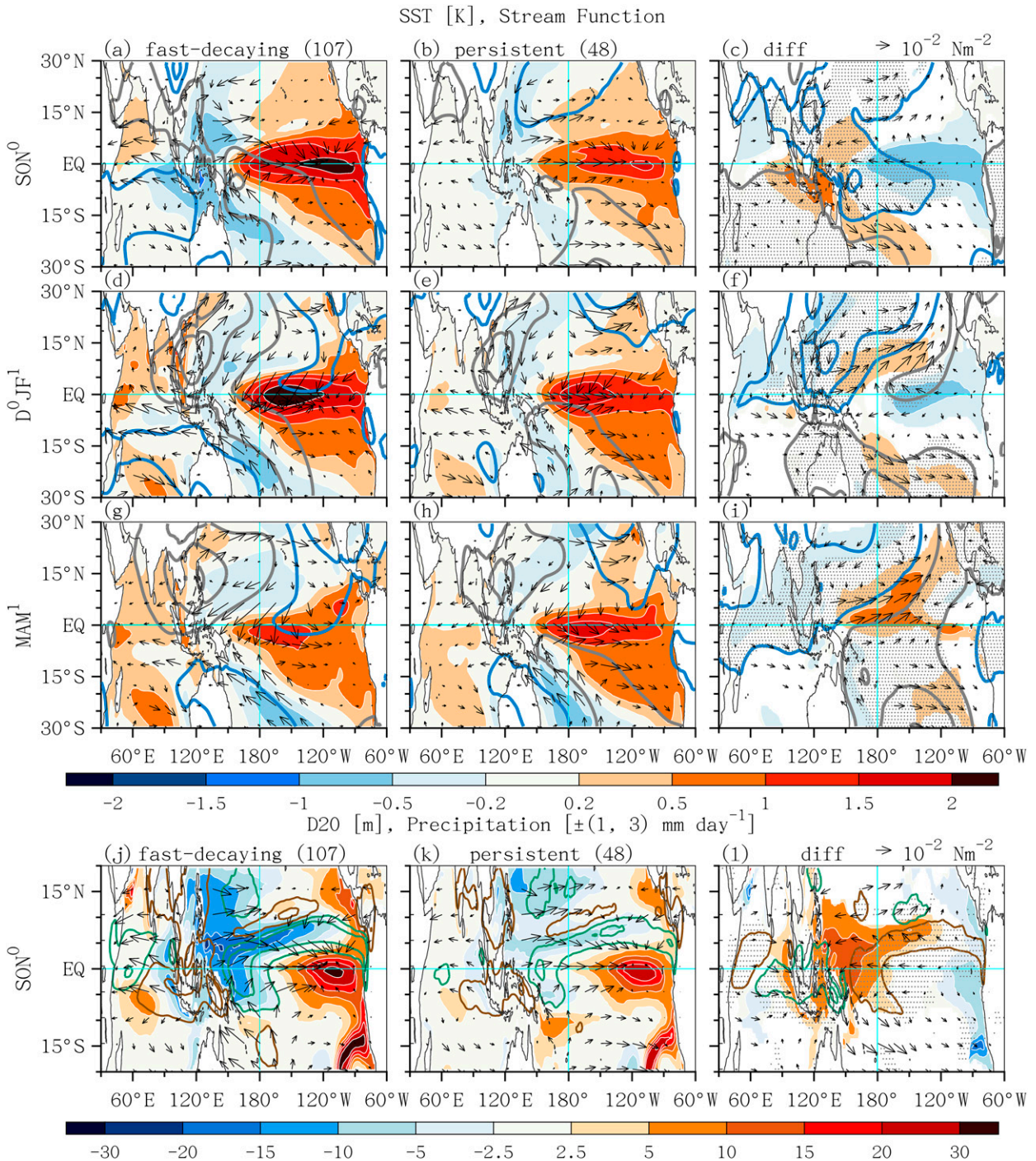
FIG. 2. Composite SST (K) (shading), 850-hPa streamfunction (contours), and surface wind stress (vector) anomalies for (left) fast-decaying events and (center) persistent events, and (right) their differences, during (a)–(c) SON^0, (d)–(f) D^0JF^1, and (g)–(i) MAM^1. Contours are plotted at $\pm(1, 2.5, 4) \times 10^4$ N m^{-3} for fast-decaying and persistent groups and $\pm(0.5, 1.5, 2.5) \times 10^4$ N m^{-3} for the difference, with positive values in gray and negative values in blue. (j)–(l) D20 (m) (shading), precipitation (contours), and surface wind stress (vector) anomalies in SON^0. Contours are plotted at ± 1 and ± 3 mm day^{-1}, with positive values in green and negative values in brown. In (c), (f), (i), and (l), the shading and vectors are shown only where the differences are statistically significant, and the stippled area marks where the difference of contours is statistically significant at 0.99 confidence level.
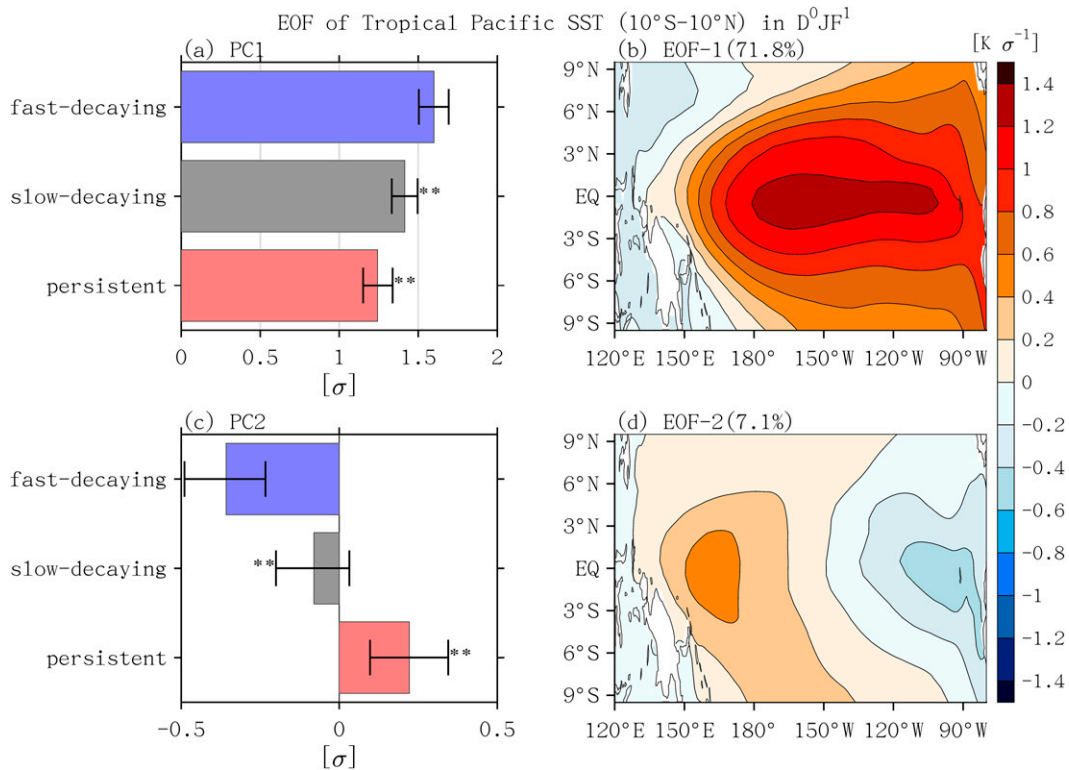
FIG. 3. The (a),(b) first and (c),(d) second EOF modes of SST anomalies over the equatorial Pacific (120°E–80°W, 10°N/S) during D^0JF^1. The bars in (a) and (c) are the averages of the principal components (std) in fast-decaying (blue), slow-decaying (gray), and persistent (red) groups, and the error bars represent the 0.99 confidence interval. The double asterisks indicate that the composite mean is significantly different from the fast-decaying group at the 0.99 confidence level. The EOF patterns (K std^{-1}) are shown in (b) and (d), and the percentages of the explained variance are shown in the panel titles.

the equatorial Pacific westerlies are weaker, and the upwelling Rossby waves are relatively unclear (Figs. 2k,l).

Note that the zonal wind anomalies over the equatorial far western North Pacific in the mature and decay stages remain positive in the persistent group but turn negative in the fast- and slow-decaying groups (Fig. 1e). For the fast-decaying group, WNPAC enhances from the growth to the mature stage (Fig. 1f) such that easterly wind anomalies on its southern flank (Figs. 1e and 2a,d) reduce the western-central Pacific westerly response to the warm Niño-3.4 SST (Fig. 1b). WNPAC appears weaker in the persistent group (Fig. 1f) and its zonal coverage is more limited to the west of 120°E in the mature stage (Fig. 2e). Such differences are consistent with the maintenance of WNPAC by the wind–evaporation–SST coupling (Wang et al. 2000; Wang and Zhang 2002) and the meridional moisture static energy transport (Wu et al. 2017a,b), as the cold SST and northerly wind anomalies over the tropical western North Pacific induced by El Niño are weaker in the persistent group (Figs. 2e,f).

The empirical orthogonal function (EOF) of the tropical Pacific (120°E–80°W, 10°N/S) SST anomalies is used to analyze El Niño's spatial diversity (Takahashi et al. 2011). We note that El Niño events of the shorter duration group tend to be the eastern Pacific (EP) type and those of the longer

duration group to be the central Pacific (CP) type. The first EOF mode (Figs. 3a,b) represents El Niño's magnitude and the second mode represents its spatial diversity (Figs. 3c,d). The relative amplitudes of the first principal component (PC1; Fig. 3a) among each group are analogous to the Niño-3.4 index (Fig. 1a), while the second mode indicates the warm SST anomaly is centered more toward the east in the fast-decaying group and the west in the persistent group (Figs. 3c,d).

In the decay stage, in addition to the persistent WNPAC, the difference pattern between the fast-decaying and persistent groups resembles the positive phase of PMM (Fig. 2i), with relaxed trade winds and the underlying warmer SST coupled in the subtropical eastern North Pacific. Previous studies have emphasized the role of the positive PMM in El Niño's initiation (e.g., Vimont et al. 2001), and here we show that the positive PMM also favors the prolonged lifetime by reinforcing tropical westerly wind anomalies.

After the mature stage, the shoaling signals at the equator propagate eastward across the basin and reach the eastern coast of the Pacific Ocean in the fast-decaying group (Fig. 4a). On the other hand, the equatorial thermocline anomalies in the persistent group (Fig. 4c) last from the latter half of year^0 through year^1 in the persistent group. In the slow-decaying group, shallower thermocline depth anomalies also propagate
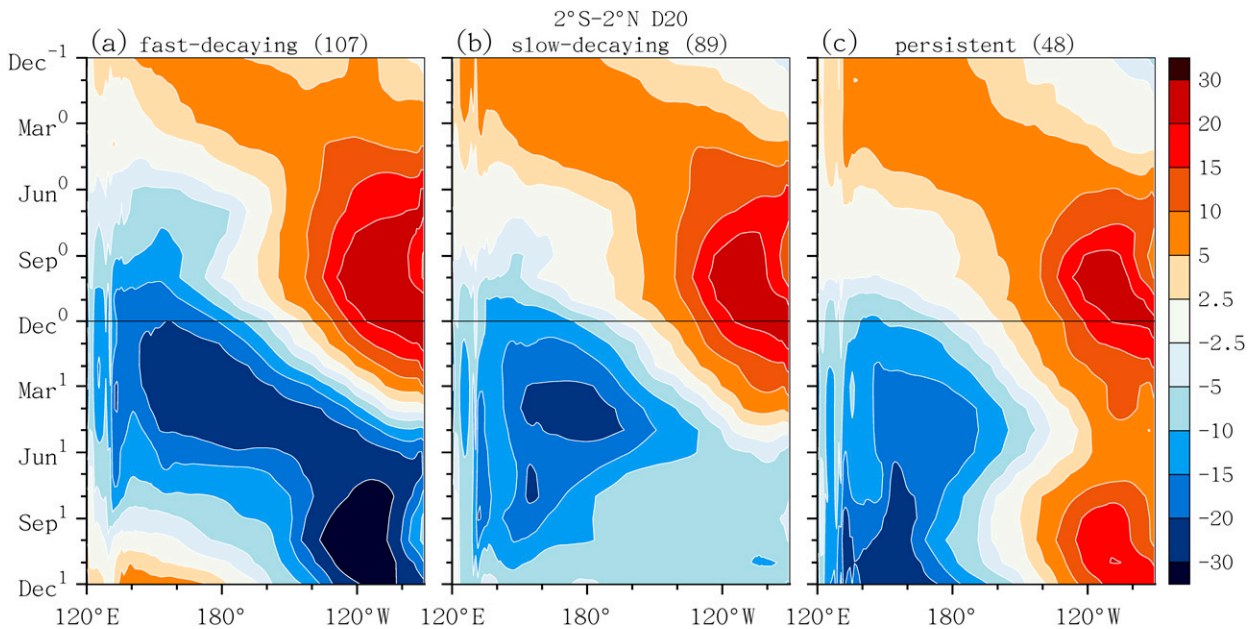
FIG. 4. D20 anomalies averaged over 2°S–2°N as a function of time and longitude for (a) fast-decaying, (b) slow-decaying, and (c) persistent events.

eastward and reach the eastern boundary in summer but are relatively weaker in comparison with the fast-decaying group (Fig. 4b). The distinct evolutions of thermocline depth anomalies in the decaying stage indicate that the strengths of upwelling Kelvin waves and WWV discharge vary from type to type.

4. Mixed layer heat budget analysis

Over the Niño-3.4 region, the evolutions of mixed layer temperature and SST anomalies are nearly identical (not shown), so it is reasonable to analyze the processes regulating the SST decay paces with the mixed layer heat budgets. The negative SST tendency emerges in the mature stage and attains the largest cooling rate in the decay stage among all three types (Fig. 1a). When the seasonal-dependent instability becomes more favorable for positive feedback in the following summer and autumn (e.g., Tziperman et al. 1997), the cold state in the fast-decaying group begins to develop and the prolonged warm state in the persistent group strengthens again. Note that although the fast-decaying type features the warmest Niño-3.4 index in the peak, it is also accompanied by the greatest cooling rate in the decay stage causing its phase transition. Hence, the mixed layer temperature change in the decay stage is crucial in determining whether the phase transition of El Niño can occur or not, and we will explore the processes corresponding to the heat budget in this section. In the next section, we will further examine why the negative feedbacks are more pronounced in the events of stronger amplitude.

The mixed layer temperature tendencies differ the most in the decay stage, with values of -0.31, -0.14, and -0.01 K month^{-1} for the fast-decaying, slow-decaying and persistent groups,

respectively (Fig. 5). In the fast-decaying group, the cooling tendency is mainly attributed to the thermodynamic processes that are mostly caused by shortwave damping (Fig. 5a). The net advection is negligible as a result of the cancellation between cooling by the zonal transport term ($-u'\overline{T}_x$) and the warming by the meridional temperature gradient ($-\overline{v}T'_y$) and meridional nonlinear ($-v'T'_y$) terms. In the persistent group, the cooling by the zonal transport term ($-u'\overline{T}_x$) is near zero, but the warming by the meridional temperature gradient term ($-\overline{v}T'_y$) contributes to the advection warming that is offset by the thermodynamic damping, resulting in the nearly zero temperature tendency. The Ekman feedback ($-w'\overline{T}_z$) and thermocline feedback ($-\overline{w}'T_z$) are relatively weak here. They are found to be more prominent in summer and autumn (e.g., M. Chen et al. 2016) when the climatological thermocline is shallower (Li and Philander 1996; Philander et al. 1996), and they do not vary much among the three types (not shown).

The distinct budget differences between the fast-decaying and persistent groups result from both dynamic and thermodynamic processes (Fig. 5d); the zonal transport term ($-u'\overline{T}_x$) dominantly contributes to ~48% of the difference, while the latent heat flux (~24%) and the meridional temperature gradient ($-\overline{v}T'_y$; ~20%) terms play a secondary role. Intriguingly, the zonal transport ($-u'\overline{T}_x$) and latent heat flux terms are also dominant in contributing to El Niño's faster decay than La Niña's (M. Chen et al. 2016; see their Table 1). In contrast, the budget difference between the fast- and slow-decaying group is mainly attributed to the dynamic process by the $-u'\overline{T}_x$ term while the thermodynamic damping rates are relatively similar (Figs. 5a,b). Next, we will explore the reason behind the variations in $-u'\overline{T}_x$, latent heat, and $-\overline{v}T'_y$ terms.

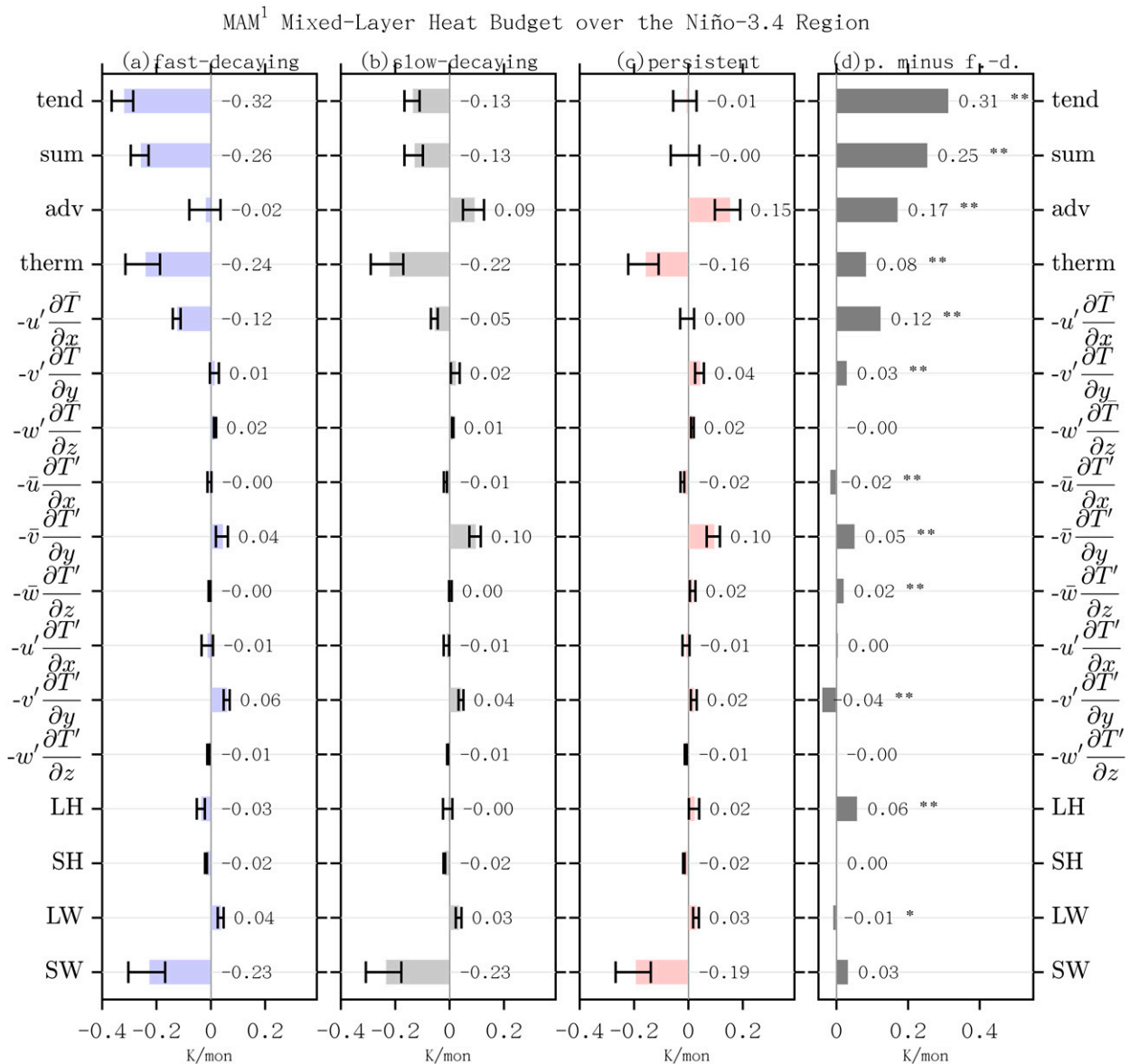MAM[1] Mixed-Layer Heat Budget over the Niño-3.4 Region

FIG. 5. The mixed layer temperature budget terms for (a) fast-decaying, (b) slow-decaying, (c) and persistent types of El Niño in the Niño-3.4 region (170°–120°W, 5°S–5°N) during MAM[1], and (d) the difference between (c) and (a). Here "sum" represents the sum of all of the terms in Eq. (1), "adv" represents dynamic processes, which is the sum of the first nine terms in Eq. (1), and "therm" represents thermodynamic processes, which is the sum of the last four terms in Eq. (1). The error bars in (a)–(c) show the ranges of the first and third quartiles in each type. In (d), double and single asterisks denote where the difference is statistically significant at the 0.99 and 0.9 confidence level, respectively.

The magnitude of the zonal transport term $(-u'\overline{T}_x)$ is determined by the zonal current anomalies shown in Table 1. In the decay stage, the subsurface cold temperature anomalies extending from the western Pacific indicate upwelling Kelvin waves, which are relatively weaker in the slow-decaying and persistent groups (Fig. 6). They shoal equatorial thermocline depth (Fig. 4). The meridional concavity of thermocline depth changed by the upwelling Kelvin waves can induce geostrophic currents [Eq. (2)]. The geostrophic component (u_g)

dominates the current anomalies as the zonal wind stress and the Ekman component (u_e) are still eastward in this season. The filtering by the equatorial wave meridional structures [Eqs. (4.1) and (4.2); Boulanger and Menkes 1995] indicates that the Kelvin wave component causes greater current differences among types than the Rossby wave component. The relatively stronger Rossby wave component in the persistent group might result from its more symmetric wind pattern about the equator than the other groups during the mature

TABLE 1. The currents and surface wind stress averaged over 120°–170°W, 5°S–5°N in MAM[1]; u, u_g, u_e, τ^x, u_{Kelvin}, and u_{Rossby} represent the composite mean zonal current, estimated geostrophic component, estimated Ekman component, surface zonal wind stress, Kelvin wave–filtered component, and Rossby wave–filtered component, respectively. Equation (2) is used for the estimation of Ekman and geostrophic currents, and Eqs. (4.1) and (4.2) are the meridional structures used to filter Kelvin and Rossby waves, respectively.

	u (10^{-2} m s^{-1})	u_g (10^{-2} m s^{-1})	u_e (10^{-2} m s^{-1})	τ^x (10^{-2} N m^{-2})	u_{Kelvin} (10^{-2} m s^{-1})	u_{Rossby} (10^{-2} m s^{-1})
Fast decaying	−13.7	−9.4	0.4	0.5	−12.2	−2.1
Slow decaying	−3.7	−6.4	1.0	0.9	−2.9	2.3
Persistent	2.1	3.7	1.3	1.0	2.3	4.0

and decay stages (Figs. 2d–i.) It is concluded that the distinct zonal transport term ($-u'\overline{T}_x$) results from the Kelvin wave–induced current anomalies.

The latent heat flux anomalies can be estimated with the bulk formula and decomposed to the specific humidity gradient, wind speed, and nonlinear terms [Eq. (3)]. The specific humidity gradient term plays a damping role in all three groups (Figs. 7a–c), as El Niño's warm SST anomalies enhance the gradient with increased surface saturation specific humidity and causes more evaporation. However, this cooling effect is largely offset by the wind speed term in the persistent and slow-decaying groups (Figs. 7b,c). In the persistent group, the tropical westerly wind anomalies are relatively symmetric about the equator and suppress the evaporation by reducing
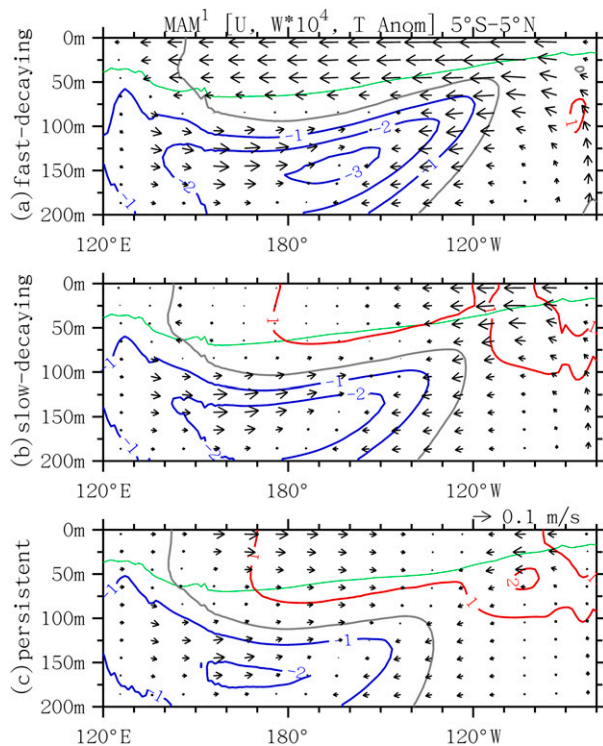

FIG. 6. The zonal-depth cross section of oceanic current (vectors) and temperature (contours; K) anomalies averaged over 5°N/S for (a) fast-decaying, (b) slow-decaying, and (c) persistent event composites during MAM[1]. The negative and positive contours are blue and red, respectively. The vertical current is multiplied by a factor of 10[4].

the climatological trade wind speeds (Fig. 7e). In comparison, the feature of the southward shift of westerly wind anomalies (e.g., McGregor et al. 2012, 2013) is more pronounced in the fast-decaying group. Its tropical wind pattern is relatively asymmetric, being northeasterly in the north and northwesterly in the south crossing the equator (Fig. 7d). This difference pattern in winds and latent heat fluxes (Fig. 7f) appears coupled to the underlying SST, resembling the positive phase of PMM (Fig. 2i), and the associated wind speed anomalies counteract the latent heat damping.

The meridional temperature gradient term ($-\overline{v}T'_y$) exerts positive feedback because the mean meridional flow diverges poleward on the upper branch of the subtropical cell (STC; McCreary and Lu 1994) and amplifies the SST anomalies centered at the equator. The warm SST in the fast-decaying group is weaker than the others during the decay stage (Fig. 1a). As a result, the meridional temperature gradient term ($-\overline{v}T'_y$) during the decay stage is less capable of maintaining the warm SST in the fast-decaying group (Fig. 5). To understand what controls the strengths of El Niño's warm SST in the decay stage, we need to further trace back to the heat budget in the mature stage.

In the mature stage, the fast-decaying group has a stronger cooling tendency (−0.12 K month^{-1}) than the slow-decaying (−0.03 K month^{-1}) and persistent groups (0.00 K month^{-1}), and it is dominated by the larger cloud-shortwave cooling in the fast-decaying (−0.22 K month^{-1}) than in the slow-decaying (−0.12 K month^{-1}) and persistent groups (−0.05 K month^{-1}). In the tropics, the pattern of decreased shortwave radiation anomalies closely follows the distribution of increased precipitation anomalies as a shadowing effect by clouds (Figs. 8a–c). As the fast-decaying group tends to be the EP type (Fig. 3), its warm SST and positive precipitation anomalies extend more eastward, and it enhances the shortwave damping more than the other groups (Fig. 8). As a result, the Niño-3.4 anomaly in the fast-decaying group exhibits a large negative tendency from the mature to decay stage (Fig. 1a). This negative SST–cloud–shortwave radiation feedback in the mature stage leaves its impact on the cooling difference in the decay stage via the meridional temperature gradient ($-\overline{v}T'_y$) term (Fig. 5).

5. Factors controlling the strength of upwelling Kelvin waves

In section 4, the zonal transport term ($-u'\overline{T}_x$) dominant in the mixed layer temperature budget difference (Fig. 5) is caused by the zonal current anomalies associated with
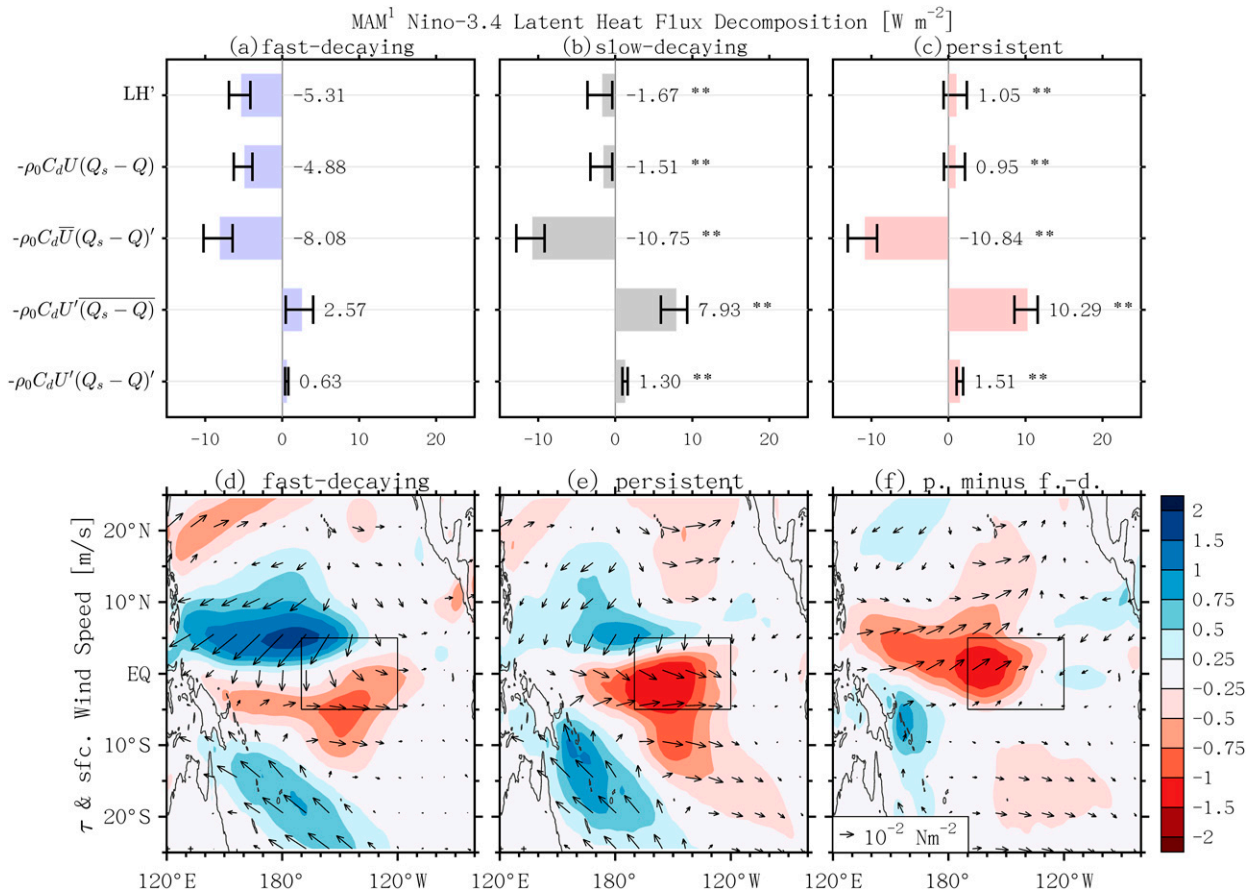
FIG. 7. Latent heat flux anomalies (LH′) in the Niño-3.4 region (170°–120°W, 5°S–5°N) during MAM[1], giving LH′, bulk formula estimation $[-\rho_0 C_d U(Q_s - Q)]$, and decomposition as specific humidity gradient $[-\rho_0 C_d \overline{U}(Q_s - Q)']$, wind speed $[-\rho_0 C_d U'\overline{(Q_s - Q)}]$, and nonlinear $[-\rho_0 C_d U'(Q_s - Q)']$ (W m^{-2}) terms averaged for the (a) fast-decaying, (b) slow-decaying, and (c) persistent groups. Mean values are shown as thick color bars, and the 99% confidence intervals are shown as thin error bars. Also shown are composite wind speed (shading; m s^{-1}) and surface wind stress (vectors) anomalies in MAM[1] for (d) fast-decaying and (e) persistent event composites, and (f) their difference. Red shadings are reduced wind speeds that act to heat up oceanic temperature, and blue shadings are enhanced wind speeds that act to cool down oceanic temperature See also Eq. (3) for decomposition.

upwelling Kelvin waves (Fig. 6; Table 1). The upwelling Kelvin wave can result from reflected equatorial Rossby waves induced in the developing seasons (Fig. 2j) or equatorial easterly wind anomalies emerging from the western Pacific as WNPAC strengthens (Fig. 2d). As they represent delayed response to El Niño's wind anomalies, they are more prominent in strong events causing more drastic event termination. In this section, we quantitatively compare the reflected waves and direct wind forcing in El Niño events. To identify Kelvin waves, first, we project D20 anomalies on the meridional structure of the theoretical Kelvin wave over 15°S–15°N [Eq. (4.1)]. The D20 field reconstructed from the spatial filtering is shown in Fig. 9, and it shows that from the mature to decay stage, the thermocline depth over the equatorial eastern Pacific is raised by about 10–15 m in the fast-decaying group, but only about 5 m in the persistent group (Figs. 9g,h). This change over time is considered the accumulation of shoaling by Kelvin waves. We define the proxy for Kelvin wave (D20$_{Kelvin}$) as the reconstructed D20 field averaged over

150°–90°W, 15°S–15°N in MAM[1] minus D[0]JF[1], where the fast-decaying and persistent groups show the greatest contrast.

Next, from each El Niño event, the Kelvin wave proxy forms a series. We calculate the correlations of the Kelvin wave proxy series with the reconstructed fields of D20 [filtered by the Rossby wave structure; Eq. (4.3)] and surface zonal wind stress [filtered by the Kelvin wave structure; Eq. (4.1)] at different lead months (Figs. 10 and 11). These correlation maps are used to identify the key regions and timing of equatorial Rossby waves and equatorial easterly wind anomalies.

The equatorial Rossby waves associated with the Kelvin wave proxy emerges along ~6°N from late summer (~August[0]) over the western-central Pacific, and grow to their peaks in the El Niño's mature stage (~January[1]–February[1]; Figs. 10a–i). As for the zonal wind stress anomalies associated with the oceanic Kelvin wave proxy, the positive correlations develop over the equatorial far western Pacific around late autumn (~November[0]) and reach full strength in late winter
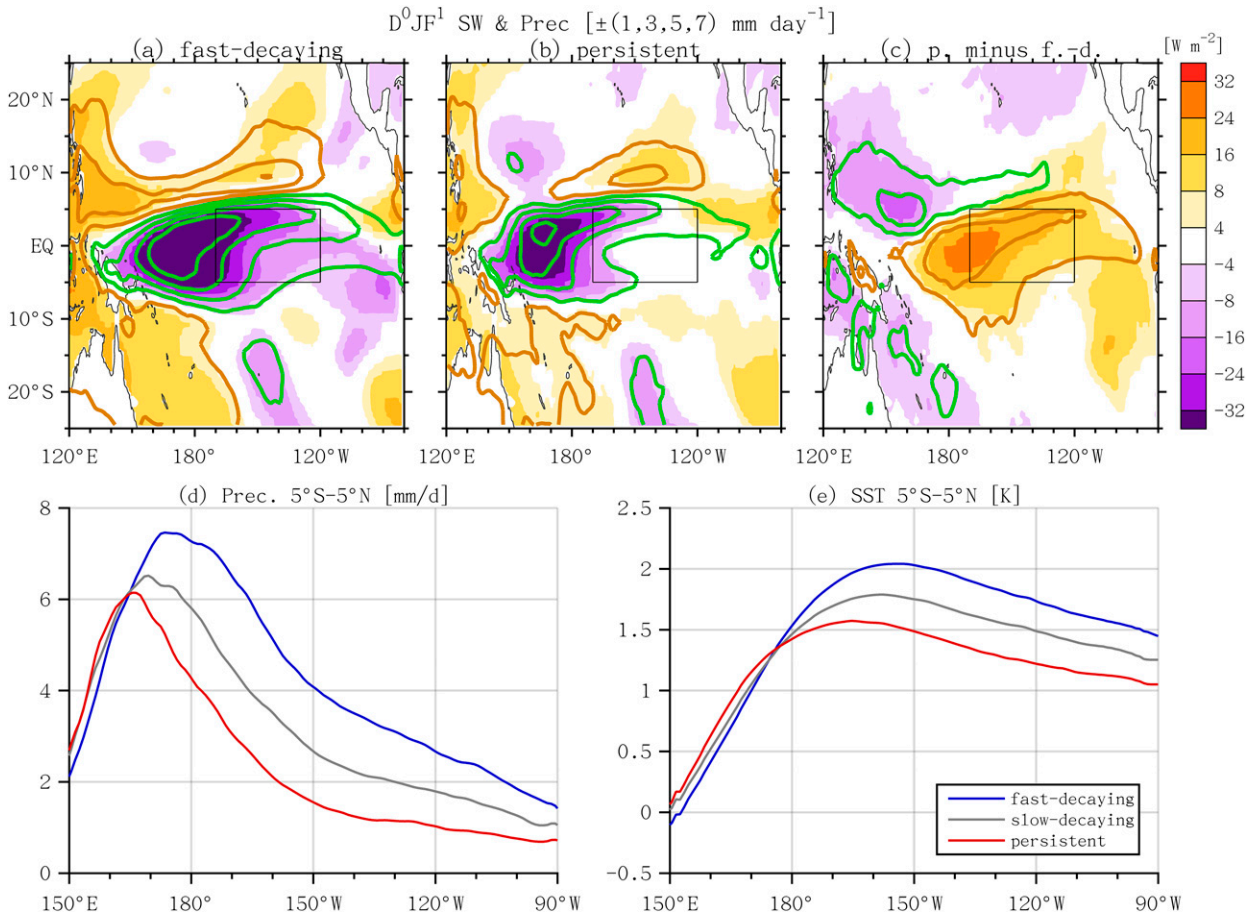
FIG. 8. Composite surface shortwave flux (shading; W m^{-2}) and precipitation (contours) anomalies for (a) fast-decaying, (b) slow-decaying, and (c) persistent groups in D^0JF^1. Contours are plotted at $\pm(1, 3, 5, 7)$ mm day^{-1} in green (positive) and brown (negative). Also shown are (d) precipitation and (e) SST anomalies averaged along 5°N/S in D^0JF^1. Blue, gray, and red curves represent the composite mean of fast-decaying, slow-decaying, and persistent events, respectively.

(~February[1]; Figs. 11a–l). The area of positive correlations continues to expand eastward toward the central Pacific in the subsequent seasons.

Based on the lead correlation patterns, the index for the reflected waves ($D20_{Rossby}$) is defined as the reconstructed D20 field averaged over 130°E–180°, 15°N/S in D^0JF^1 (Fig. 10j), and the index for the wind stresses (τ^x_{Kelvin}) is defined as the reconstructed zonal wind stress field over 120°E–150°, 15°S–15°N in JFM[1] (Fig. 11m). We also add Niño-3.4 SST and WNPAC streamfunction (defined as in section 3 and Fig. 1) at the growth (SON^0) and mature (D^0JF^1) stages, respectively, as key variables to the intercomparison on scatter diagrams (Fig. 12).

The scatterplot confirms that stronger upwelling Rossby waves occur in the events with warmer Niño-3.4 amplitudes (Fig. 12a), which correlate to stronger upwelling Kelvin waves in the later stage (Fig. 12d). WNPAC is positively correlated to the SON^0 Niño-3.4 index (Fig. 12b) and the western Pacific easterly wind anomalies (Fig. 12c), and the easterly wind anomalies correlate to stronger upwelling Kelvin waves as well (Fig. 12e). That is, both sources of forcing for upwelling

Kelvin waves (i.e., easterly wind and reflected waves) are more favored in early onset events. Fast-decaying and persistent events tend to be located at the opposite sides of the scatter diagrams, though not completely separated. Here, we show that the stronger amplitude of El Niño correlates to stronger negative feedback that dominantly differentiates the decay rates of events via air–sea coupled interactions.

Next, we compare the contribution of Rossby waves and easterly wind to Kelvin waves with partial correlation analysis as

$$\rho_{KR(Z)} = \frac{\rho_{KR} - \rho_{KZ}\rho_{RZ}}{\sqrt{1 - \rho^2_{KZ}}\sqrt{1 - \rho^2_{RZ}}} \quad \text{and} \quad (5.1)$$

$$\rho_{KZ(R)} = \frac{\rho_{KZ} - \rho_{KR}\rho_{RZ}}{\sqrt{1 - \rho^2_{KR}}\sqrt{1 - \rho^2_{RZ}}}. \quad (5.2)$$

The terms ρ_{KR}, ρ_{KZ}, and ρ_{RZ} are the correlation coefficients between $D20_{Kelvin}$ and $D20_{Rossby}$, between $D20_{Kelvin}$ and τ^x_{Kelvin}, and between $D20_{Rossby}$ and τ^x_{Kelvin}, respectively; $\rho_{KR(Z)}$
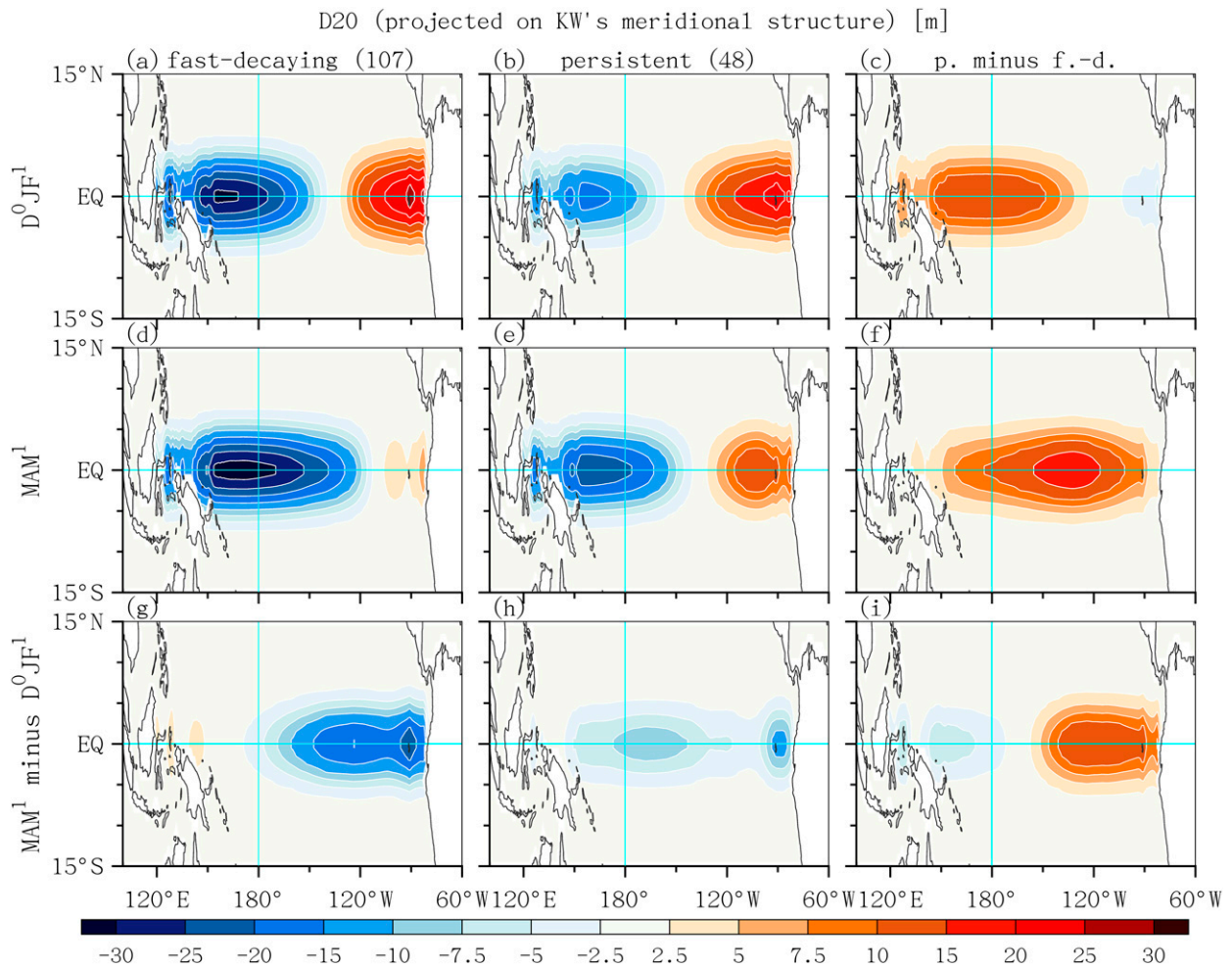
FIG. 9. Composite fields of Kelvin-wave-filtered D20 anomalies for the (left) fast-decaying events and (center) persistent events, and (right) their differences, in (a)–(c) D^0JF^1 and (d)–(f) MAM^1, and (g)–(i) changes in time $MAM^1 - D^0JF^1$.

represents the partial correlation coefficient between Kelvin wave and Rossby waves when the zonal wind stress is controlled, and $\rho_{KZ(R)}$ represents the partial correlation coefficient between Kelvin wave and zonal wind stress when the Rossby wave is controlled. It turns out they both contribute to Kelvin waves comparably, with $\rho_{KR(Z)}$ being 0.43 and $\rho_{KZ(R)}$ being 0.42.

6. Summary

A total of 244 El Niño events in a 1200-yr piControl simulation from CMIP6 CESM2 are classified to the fast-decaying (107), slow-decaying (89), and persistent (48) groups based on their Niño-3.4 SST evolutions. After the mature winter, the fast-decaying group rapidly terminate before the ensuing summer and develops as a La Niña event, the slow-decaying group decays to the neutral state with a relatively gradual pace, and the persistent group barely weakens and reaches another peak in the following winter. The fast-decaying and persistent groups are distinct from each other, while the slow-

decaying group is in between. The main mechanisms for the El Niño evolution leading to the persistent events relative to the fast-decaying ones are summarized in Fig. 13.

In spring and summer during the development stage, all three groups are preconditioned by a similar amount of positive WWV anomalies (Fig. 1d). Relative to the persistent events, the fast-decaying events develop earlier in the growth stage (SON^0; Figs. 1a–c) as in observations with stronger westerly wind anomalies over equatorial Pacific driven by tropical atmospheric heating/cooling distribution related to El Niño–pIOD SST, and upwelling Rossby waves forced by equatorial westerlies (Figs. 2a,j). In contrast, the equatorial westerly wind stresses and Rossby waves are less prominent in the persistent events because of the later development of El Niño and the absence of pIOD (Figs. 2k,l). The far western North Pacific zonal wind anomalies turn easterly in the fast-decaying events but remain westerly in the persistent events (Fig. 1e) resulting from WNPAC during the mature stage (D^0JF^1; Figs. 1f and 2d–f). After the decay stage (MAM^1), negative D20 anomalies caused by the preceding equatorial
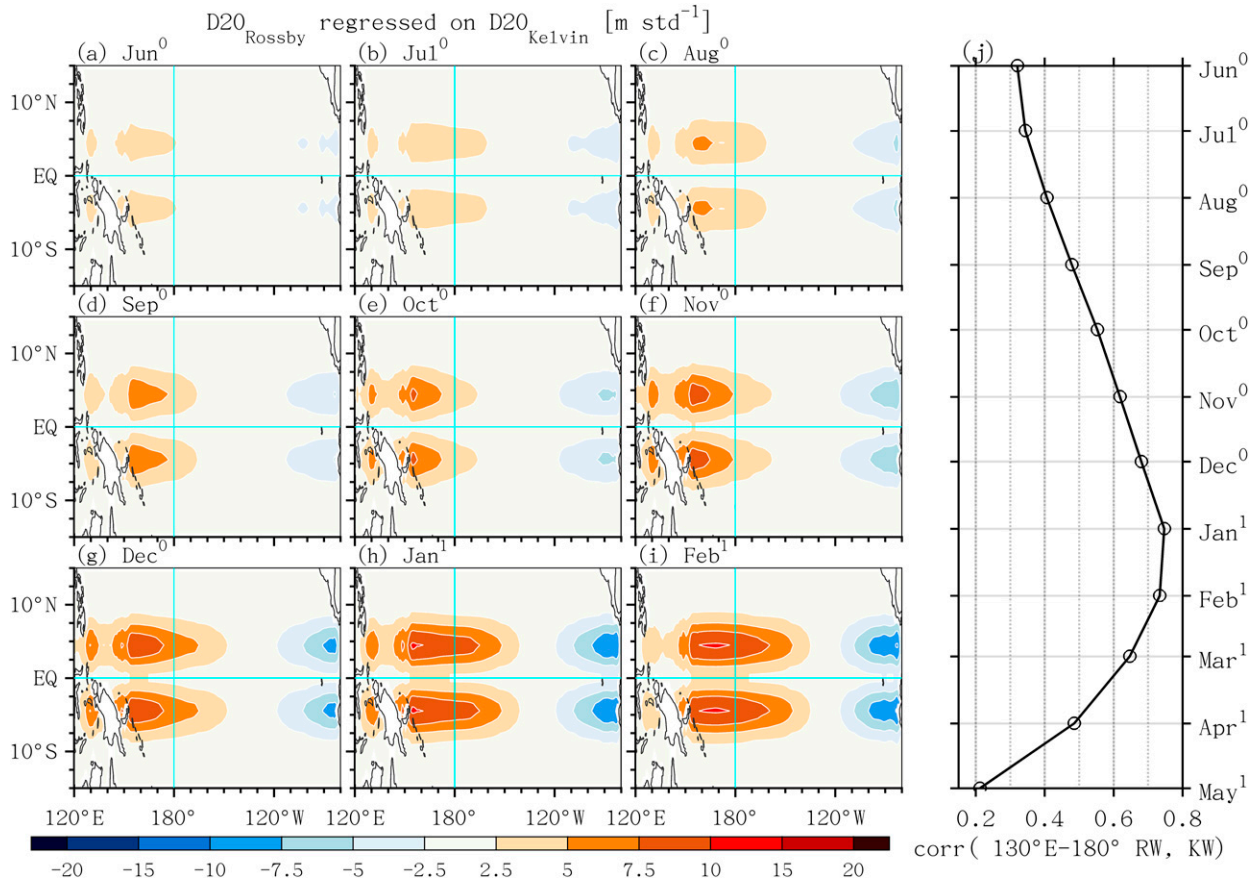
FIG. 10. (a)–(i) The lead correlation of the Kelvin wave proxy (D20$_{Kelvin}$) with the Rossby-wave-filtered D20 anomalies at lead months from June[0] to February[1], respectively, and (j) spatially averaged lead correlation in (a)–(i) within 130°E–180°. D20$_{Kelvin}$ is defined as the tendency change of KW spatial-filtered D20 (MAM[1] − D[0]JF[1]) averaged within 150°–90°W, 15°S–15°N. See Fig. 9 and section 5 for more details.

Rossby waves and the WNPAC-related easterly winds propagate eastward across the basin as Kelvin waves and terminate the fast- and slow-decaying groups of events, whereas the eastward-tilting thermocline anomalies are relatively stationary in the persistent events (Fig. 4) and maintain the positive atmosphere–ocean feedbacks in year[1] (Figs. 1a–c). The discharge of WWV is also fastest (slowest) in the fast-decaying (persistent) group during the mature and decay stages (Fig. 1d).

Among the three duration types, the SST tendency differs the most during the decay stage that determines whether the Niño-3.4 SST turns to the opposite phase in the latter half of year[1] (Fig. 1a). The leading contributions to the heat budget difference between the fast-decaying and persistent groups are zonal transport ($-u'\overline{T}_x$; ~48%), latent heat (~24%), and meridional temperature gradient ($-\overline{v}T'_y$; ~20%) terms (Fig. 5). The zonal transport cooling driven by the Kelvin-wave-related westward currents is strong (weak) in fast-decaying (persistent) events (Fig. 6; Table 1). Latent heat usually plays a dampening role as the moisture gradient increases with warm SST, but the positive PMM appears in the persistent group and suppresses the evaporation cooling by reducing the northeasterly trade winds (Fig. 7). The warm SST decreases

from the mature to decay stage more in the fast-decaying than persistent events (Fig. 1a) due to the negative SST–cloud–shortwave radiation feedback (Fig. 8) spatially distributed similar to EP and CP El Niño, respectively. Thus, the meridional temperature gradient term ($-\overline{v}T'_y$) is more capable of maintaining the warm SST in the persistent group than the fast-decaying one (Fig. 5).

Last, we project D20 and wind fields onto their theoretical meridional structures [Eq. (4)] and reconstruct them to quantify the relative contributions by the preceding equatorial Rossby waves (Fig. 10) and the anomalous equatorial western Pacific easterly wind anomalies (Fig. 11) to the upwelling Kelvin waves (Fig. 9). Both the upwelling Rossby waves and WNPAC-induced easterly wind anomalies are more prominent in earlier onset events, and their contributions to the upwelling Kelvin waves are comparably crucial (Fig. 12). This delayed negative feedback of upwelling Kelvin wave to El Niño's wind and SST anomalies explains why stronger events are accompanied by greater cooling paces in the decay stage.

Previous studies have shown that the pIOD in the developing autumn (Kim and Yu 2020), reflected Rossby waves and western Pacific easterly winds in the decaying spring (Wu et al. 2019)
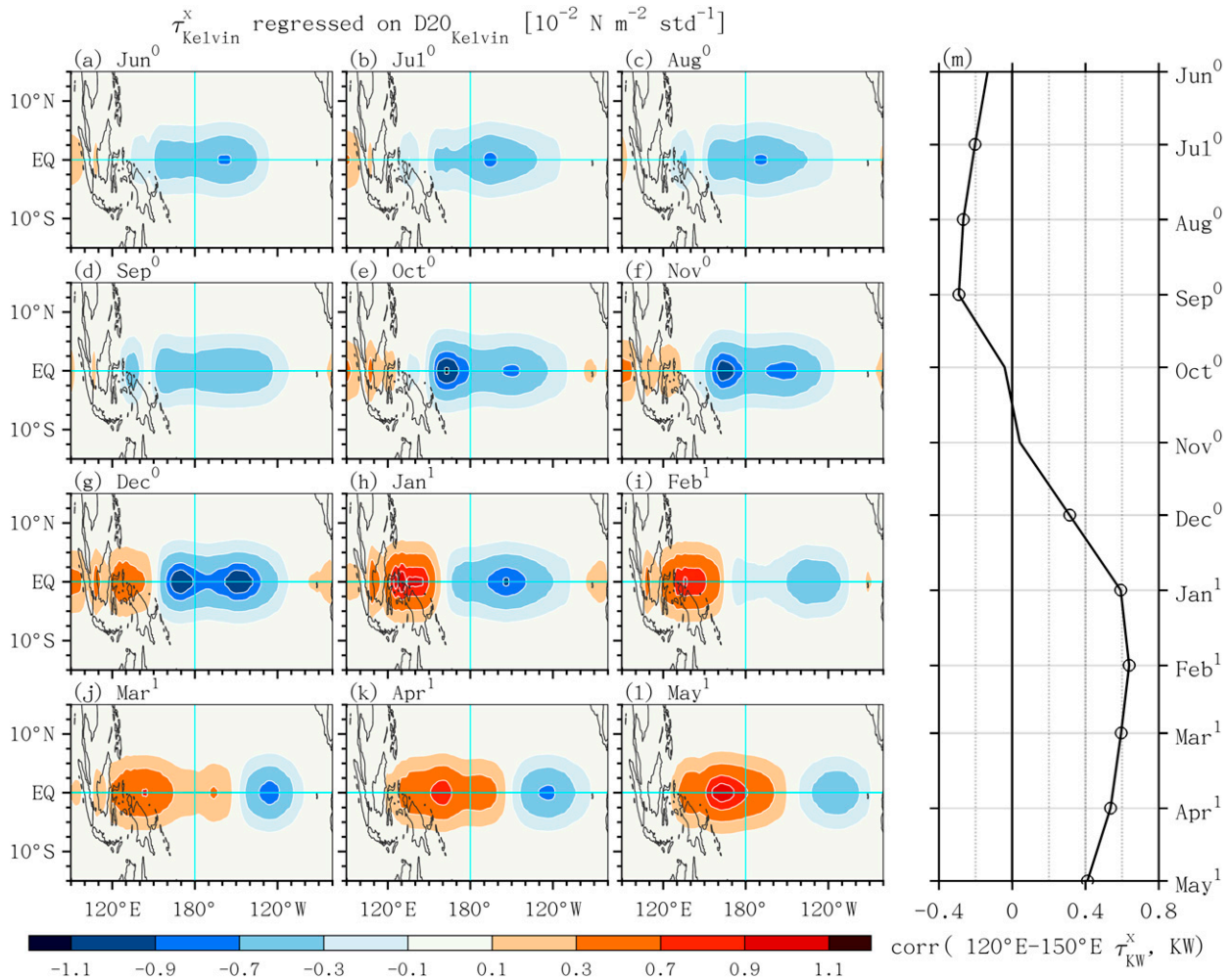
FIG. 11. (a)–(l) The lead correlation of the Kelvin wave proxy (D20$_{Kelvin}$) with the Kelvin-wave-filtered surface zonal wind stress anomalies at lead months from June^0 to May^1, respectively, and (m) spatially averaged lead correlation in (a)–(l) within 120°–150°E. D20$_{Kelvin}$ is defined as tendency change of KW spatial-filtered D20 (MAM^1 − D^{0}JF^1) averaged within 150°–90°W, 15°S–15°N. See Fig. 9 and section 5 for more details.

could hasten El Niño's phase transition, whereas the negative NPO in mature winter (Wu et al. 2019; Kim and Yu 2020) and CP-type SST distribution (Ding et al. 2022) could slow down El Niño's decay. Here, we quantify their relative roles in regulating El Niño's decay pace. Our analysis of major cooling processes reveals that the impact of the upwelling Kelvin wave is about twice as much as that of the Pacific meridional mode (PMM) or El Niño's central Pacific/eastern Pacific (CP/EP) flavor, while the strength of upwelling Kelvin waves is equally attributed to reflected waves and wind forcing (Fig. 13).

7. Discussion

In consistency with the previous observation and modeling studies (Wu et al. 2019; Lee et al. 2020), in CESM2, El Niño events of a prolonged duration tend to develop later in the first year. Our results suggest that this relationship exists because the primary process regulating the cooling tendency, the Kelvin wave–induced cold zonal advection, arises from reflected equatorial Rossby waves and equatorial western Pacific easterly wind anomalies of WNPAC forced by El Niño in the developing and mature stages. Therefore, strong events with warmer peaks are terminated more drastically and El Niño's onset timing and duration are dependent on each other to some degree. However, this linear relationship can be loose as thermodynamic processes in the winter and spring are relatively unrelated to El Niño's amplitudes in the development stage. Instead, the shortwave damping is associated with the zonal distribution of SST and precipitation, and additional latent heat warming can be caused by a relatively symmetric wind pattern about the equator, such as the PMM. Our result consolidates the existing literature and provides a more comprehensive and physical pathway for the causality chain between El Niño's onset timing and duration that awaits validation in further studies.

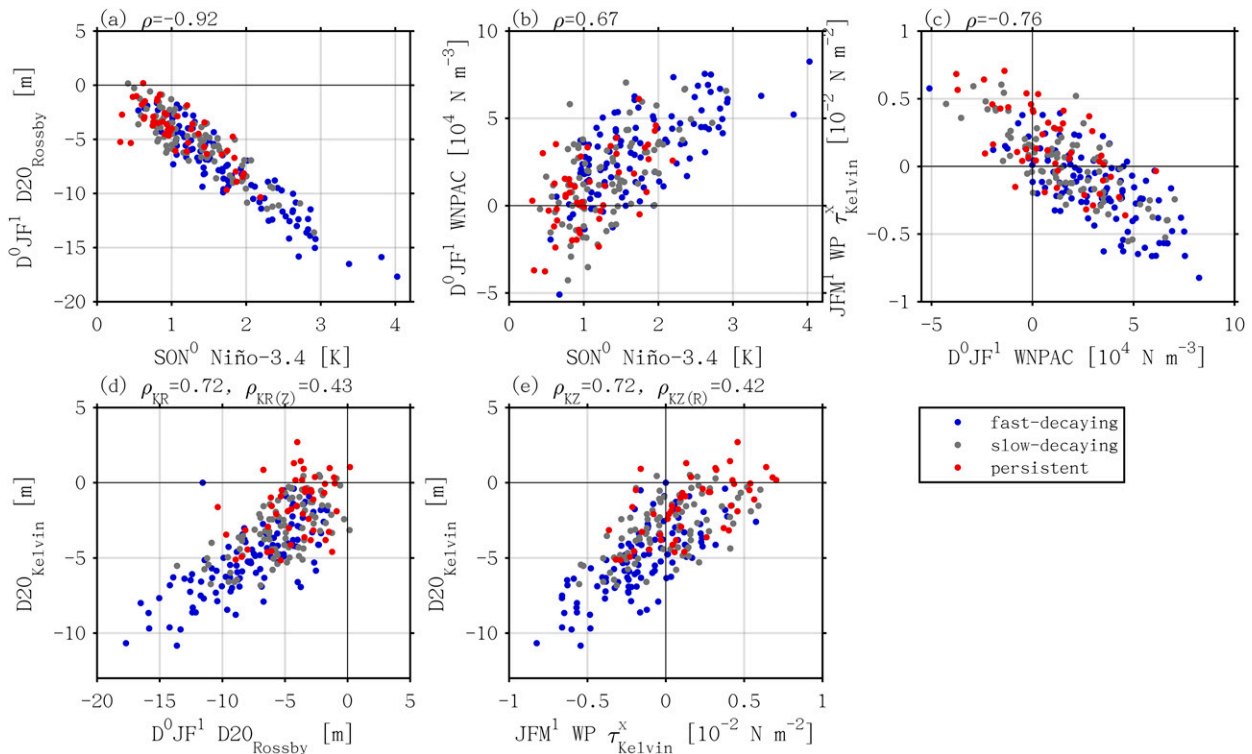What determines the onset timing of El Niño? In CESM2, the SST tendencies during the growth (year^0) are similar in

FIG. 12. The scatterplots for (a) D^0JF^1 equatorial Rossby wave (m) vs SON^0 Niño-3.4 index (K), (b) D^0JF^1 WNPAC streamfunction (10^4 N m^{-3}) vs SON^0 Niño-3.4 index (K), (c) JFM^1 far equatorial western Pacific surface zonal wind stress anomalies (10^{-2} N m^{-2}) vs D^0JF^1 WNPAC streamfunction (10^4 N m^{-3}), (d) Kelvin wave (m) vs equatorial Rossby wave (m), and (e) Kelvin wave (m) vs equatorial far western Pacific zonal wind stress anomalies (10^{-2} N m^{-2}). Blue, gray, and red dots are fast-decaying, slow-decaying, and persistent events, respectively. The correlation coefficients ρ are shown in panel titles, and the partial correlation coefficients for (d) and (e) are also shown. The partial correlation coefficients are calculated as in Eq. (5); see Figs. 1, 7, 8, and 9 and section 5 for the definition of each index.

any duration types of events (Fig. 1a) as our definition only depends on the decay rate. This indicates the El Niño's amplitude in the development stage is mainly determined by the initial state in the previous year; that is, the later-onset persistent El Niño follows a previous La Niña–like condition, while the early-onset fast-decaying event emerges from a neutral condition. With the observed prolonged El Niño events, Lee et al. (2020) showed that an enhanced climatological cross-hemisphere meridional SST gradient and cross-equatorial southerly over eastern Pacific in summer and autumn can disrupt Bjerknes feedback (Bjerknes 1969), as the equatorward shift of ITCZ precipitation is hindered. This feature is also noted in CESM2 but of less statistical significance (Figs. 2b,c,k,l). The meridional gradient of SST over subtropical eastern Pacific during both the developing and decaying stages (e.g., PMM) appear to affect El Niño's evolution, and their interaction may help understand El Niño's diverse temporal characteristics under different climate backgrounds.

The easterly wind anomalies critical for the phase transition begin from the warm pool in the mature winter, and this study highlights the role of WNPAC (e.g., Wang et al. 1999, 2000; Wang and Zhang 2002) in the East Asian winter monsoon regime. Via heating/cooling over the Maritime Continent and the western North Pacific, ENSO's evolution can be affected by Asian monsoon interannual variability. For example,

during a phase of suppressed Indian summer rainfall in the tropical biennial oscillation (e.g., Meehl 1994, 1997), if the associated cooling anomalies induce anomalous tropical easterly winds and positive IOD that strengthens subsidence over the Maritime Continent (Li et al. 2006), it can cause a stronger El Niño and WNPAC response in the mature winter and leads to a faster phase transition. The impact of the Asian–Australian monsoon on ENSO duration requires further study.
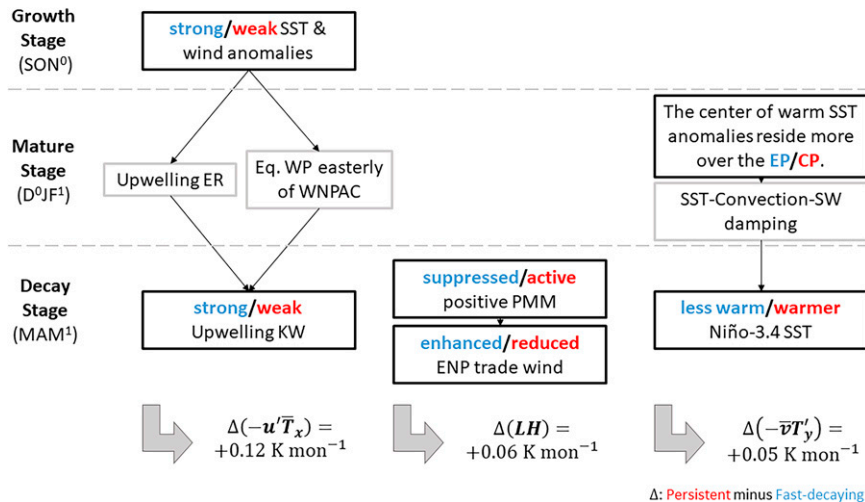
FIG. 13. A schematic diagram summarizing the key variables and processes that differentiate the cooling tendency during the decaying spring (MAM^1) for the fast-decaying group (blue) and persistent group (red) of El Niño. Here ER indicates equatorial Rossby waves, KW is Kelvin waves, WP is western Pacific, PMM is Pacific meridional mode, ENP is eastern North Pacific, LH is latent heat, and SW is shortwave radiation.

REFERENCES

Alexander, M. A., D. J. Vimont, P. Chang, and J. D. Scott, 2010: The impact of extratropical atmospheric variability on ENSO: Testing the seasonal footprinting mechanism using coupled model experiments. *J. Climate*, **23**, 2885–2901, https://doi.org/10.1175/2010JCLI3205.1.

Anderson, B. T., R. C. Perez, and A. Karspeck, 2013: Triggering of El Niño onset through trade wind-induced charging of the equatorial Pacific. *Geophys. Res. Lett.*, **40**, 1212–1216, https://doi.org/10.1002/grl.50200.

Battisti, D. S., and A. C. Hirst, 1989: Interannual variability in a tropical atmosphere–ocean model: Influence of the basic state, ocean geometry and nonlinearity. *J. Atmos. Sci.*, **46**, 1687–1712, https://doi.org/10.1175/1520-0469(1989)046<1687:IVIATA>2.0.CO;2.

Bjerknes, J., 1969: Atmospheric teleconnections from the equatorial Pacific. *Mon. Wea. Rev.*, **97**, 163–172, https://doi.org/10.1175/1520-0493(1969)097<0163:ATFTEP>2.3.CO;2.

Boulanger, J.-P., and C. Menkes, 1995: Propagation and reflection of long equatorial waves in the Pacific Ocean during the 1992–1993 El Niño. *J. Geophys. Res.*, **100**, 25 041–25 059, https://doi.org/10.1029/95JC02956.

Capotondi, A., C. Deser, A. S. Phillips, Y. Okumura, and S. M. Larson, 2020: ENSO and Pacific decadal variability in the Community Earth System Model version 2. *J. Adv. Model. Earth Syst.*, **12**, e2019MS002022, https://doi.org/10.1029/2019MS002022.

Chang, P., L. Zhang, R. Saravanan, D. J. Vimont, J. C. H. Chiang, L. Ji, H. Seidel, and M. K. Tippett, 2007: Pacific meridional mode and El Niño–Southern Oscillation. *Geophys. Res. Lett.*, **34**, L16608, https://doi.org/10.1029/2007GL030302.

Chen, H.-C., Z.-Z. Hu, B. Huang, and C.-H. Sui, 2016: The role of reversed equatorial zonal transport in terminating an ENSO event. *J. Climate*, **29**, 5859–5877, https://doi.org/10.1175/JCLI-D-16-0047.1.

Chen, L., T. Li, B. Wang, and L. Wang, 2017: Formation mechanism for 2015/16 super El Niño. *Sci. Rep.*, **7**, 2975, https://doi.org/10.1038/s41598-017-02926-3.

Chen, M., T. Li, X. Shen, and B. Wu, 2016: Relative roles of dynamic and thermodynamic processes in causing evolution asymmetry between El Niño and La Niña. *J. Climate*, **29**, 2201–2220, https://doi.org/10.1175/JCLI-D-15-0547.1.

Chiang, J. C. H., and D. J. Vimont, 2004: Analogous Pacific and Atlantic meridional modes of tropical atmosphere–ocean variability. *J. Climate*, **17**, 4143–4158, https://doi.org/10.1175/JCLI4953.1.

Danabasoglu, G., and Coauthors, 2020: The Community Earth System Model version 2 (CESM2). *J. Adv. Model. Earth Syst.*, **12**, e2019MS001916, https://doi.org/10.1029/2019MS001916.

Di Lorenzo, E., G. Liguori, N. Schneider, J. C. Furtado, B. T. Anderson, and M. A. Alexander, 2015: ENSO and meridional modes: A null hypothesis for Pacific climate variability. *Geophys. Res. Lett.*, **42**, 9440–9448, https://doi.org/10.1002/2015GL066281.

Ding, R., and Coauthors, 2022: Multi-year El Niño events tied to the North Pacific Oscillation. *Nat. Commun.*, **13**, 3871, https://doi.org/10.1038/s41467-022-31516-9.

Dommenget, D., and Y. Yu, 2016: The seasonally changing cloud feedbacks contribution to the ENSO seasonal phase-locking. *Climate Dyn.*, **47**, 3661–3672, https://doi.org/10.1007/s00382-016-3034-6.

Eyring, V., S. Bony, G. A. Meehl, C. A. Senior, B. Stevens, R. J. Stouffer, and K. E. Taylor, 2016: Overview of the Coupled Model Intercomparison Project Phase 6 (CMIP6) experimental design and organization. *Geosci. Model Dev.*, **9**, 1937–1958, https://doi.org/10.5194/gmd-9-1937-2016.

Harrison, D. E., 1987: Monthly mean island surface winds in the central tropical Pacific and El Niño events. *Mon. Wea. Rev.*, **115**, 3133–3145, https://doi.org/10.1175/1520-0493(1987)115<3133:MMISWI>2.0.CO;2.

——, and G. A. Vecchi, 1999: On the termination of El Niño. *Geophys. Res. Lett.*, **26**, 1593–1596, https://doi.org/10.1029/1999GL900316.

Hong, C.-C., T. Li, LinHo, and J.-S. Kug, 2008: Asymmetry of the Indian Ocean dipole. Part I: Observational analysis. *J. Climate*, **21**, 4834–4848, https://doi.org/10.1175/2008JCLI2222.1.

Huang, B., and Coauthors, 2017: Extended Reconstructed Sea Surface Temperature version 5 (ERSSTv5): Upgrades, validations, and intercomparisons. *J. Climate*, **30**, 8179–8205, https://doi.org/10.1175/JCLI-D-16-0836.1.

Izumo, T., and Coauthors, 2010: Influence of the state of the Indian Ocean Dipole on the following year's El Niño. *Nat. Geosci.*, **3**, 168–172, https://doi.org/10.1038/ngeo760.

——, J. Vialard, H. Dayan, M. Lengaigne, and I. Suresh, 2016: A simple estimation of equatorial Pacific response from wind-stress to untangle Indian Ocean dipole and basin influences on El Niño. *Climate Dyn.*, **46**, 2247–2268, https://doi.org/10.1007/s00382-015-2700-4.

Jin, F.-F., 1997: An equatorial ocean recharge paradigm for ENSO. Part I: Conceptual model. *J. Atmos. Sci.*, **54**, 811–829, https://doi.org/10.1175/1520-0469(1997)054<0811:AEORPF>2.0.CO;2.

——, J. D. Neelin, and M. Ghil, 1994: El Niño on the devil's staircase: Annual subharmonic steps to chaos. *Science*, **264**, 70–72, https://doi.org/10.1126/science.264.5155.70.

Kim, J.-W., and J.-Y. Yu, 2020: Understanding reintensified multiyear El Niño events. *Geophys. Res. Lett.*, **47**, e2020GL087644, https://doi.org/10.1029/2020GL087644.

——, and ——, 2021: Evolution of subtropical Pacific-onset El Niño: How its onset location controls its decay evolution. *Geophys. Res. Lett.*, **48**, e2020GL091345, https://doi.org/10.1029/2020GL091345.

Kug, J.-S., and I.-S. Kang, 2006: Interactive feedback between ENSO and the Indian Ocean. *J. Climate*, **19**, 1784–1801, https://doi.org/10.1175/JCLI3660.1.

Larson, S., and B. Kirtman, 2013: The Pacific meridional mode as a trigger for ENSO in a high-resolution coupled model. *Geophys. Res. Lett.*, **40**, 3189–3194, https://doi.org/10.1002/grl.50571.

Lee, C.-W., Y.-H. Tseng, C.-H. Sui, F. Zheng, and E.-T. Wu, 2020: Characteristics of the prolonged El Niño events during 1960–2020. *Geophys. Res. Lett.*, **47**, e2020GL088345, https://doi.org/10.1029/2020GL088345.

Levine, A. F. Z., and M. J. McPhaden, 2016: How the July 2014 easterly wind burst gave the 2015–2016 El Niño a head start. *Geophys. Res. Lett.*, **43**, 6503–6510, https://doi.org/10.1002/2016GL069204.

Li, T., 1997: Phase transition of the El Niño–Southern Oscillation: A stationary SST mode. *J. Atmos. Sci.*, **54**, 2872–2887, https://doi.org/10.1175/1520-0469(1997)054<2872:PTOTEN>2.0.CO;2.

——, and S. G. H. Philander, 1996: On the annual cycle of the eastern equatorial Pacific. *J. Climate*, **9**, 2986–2998, https://doi.org/10.1175/1520-0442(1996)009<2986:OTACOT>2.0.CO;2.

——, and P.-C. Hsu, 2017: *Fundamentals of Tropical Climate Dynamics*. Springer, 229 pp.

——, P. Liu, X. Fu, B. Wang, and G. A. Meehl, 2006: Spatiotemporal structures and mechanisms of the tropospheric biennial oscillation in the Indo-Pacific warm ocean regions. *J. Climate*, **19**, 3070–3087, https://doi.org/10.1175/JCLI3736.1.

Maeda, S., Y. Urabe, K. Takemura, T. Yasuda, and Y. Tanimoto, 2016: Active role of the ITCZ and WES feedback in hampering the growth of the expected full-fledged El Niño in 2014. *SOLA*, **12**, 17–21, https://doi.org/10.2151/sola.2016-004.

McCreary, J. P., Jr., and P. Lu, 1994: Interaction between the subtropical and equatorial ocean circulations: The subtropical cell. *J. Phys. Oceanogr.*, **24**, 466–497, https://doi.org/10.1175/1520-0485(1994)024<0466:IBTSAE>2.0.CO;2.

McGregor, S., A. Timmermann, N. Schneider, M. F. Stuecker, and M. H. England, 2012: The effect of the South Pacific convergence zone on the termination of El Niño events and the meridional asymmetry of ENSO. *J. Climate*, **25**, 5566–5586, https://doi.org/10.1175/JCLI-D-11-00332.1.

——, N. Ramesh, P. Spence, M. H. England, M. J. McPhaden, and A. Santoso, 2013: Meridional movement of wind anomalies during ENSO events and their role in event termination. *Geophys. Res. Lett.*, **40**, 749–754, https://doi.org/10.1002/grl.50136.

McPhaden, M. J., 2015: Playing hide and seek with El Niño. *Nat. Climate Change*, **5**, 791–795, https://doi.org/10.1038/nclimate2775.

Meehl, G. A., 1994: Coupled land–ocean–atmosphere processes and South Asian monsoon variability. *Science*, **266**, 263–267, https://doi.org/10.1126/science.266.5183.263.

——, 1997: The South Asian monsoon and the tropospheric biennial oscillation. *J. Climate*, **10**, 1921–1943, https://doi.org/10.1175/1520-0442(1997)010<1921:TSAMAT>2.0.CO;2.

Meinen, C. S., and M. J. McPhaden, 2000: Observations of warm water volume changes in the equatorial Pacific and their relationship to El Niño and La Niña. *J. Climate*, **13**, 3551–3559, https://doi.org/10.1175/1520-0442(2000)013<3551:OOWWVC>2.0.CO;2.

Menkes, C. E., M. Lengaigne, J. Vialard, M. Puy, P. Marchesiello, S. Cravatte, and G. Cambon, 2014: About the role of westerly wind events in the possible development of an El Niño in 2014. *Geophys. Res. Lett.*, **41**, 6476–6483, https://doi.org/10.1002/2014GL061186.

Min, Q., J. Su, R. Zhang, and X. Rong, 2015: What hindered the El Niño pattern in 2014? *Geophys. Res. Lett.*, **42**, 6762–6770, https://doi.org/10.1002/2015GL064899.

Philander, S. G. H., D. Gu, G. Lambert, T. Li, D. Halpern, N.-C. Lau, and R. C. Pacanowski, 1996: Why the ITCZ is mostly north of the equator. *J. Climate*, **9**, 2958–2972, https://doi.org/10.1175/1520-0442(1996)009<2958:WTIIMN>2.0.CO;2.

Rasmusson, E. M., and T. H. Carpenter, 1982: Variations in tropical sea surface temperature and surface wind fields associated with the Southern Oscillation/El Niño. *Mon. Wea. Rev.*, **110**, 354–384, https://doi.org/10.1175/1520-0493(1982)110<0354:VITSST>2.0.CO;2.

Ropelewski, C. F., and M. S. Halpert, 1987: Global and regional scale precipitation patterns associated with the El Niño/Southern Oscillation. *Mon. Wea. Rev.*, **115**, 1606–1626, https://doi.org/10.1175/1520-0493(1987)115<1606:GARSPP>2.0.CO;2.

Stein, K., N. Schneider, A. Timmermann, and F.-F. Jin, 2010: Seasonal synchronization of ENSO events in a linear stochastic model. *J. Climate*, **23**, 5629–5643, https://doi.org/10.1175/2010JCLI3292.1.

Stuecker, M. F., A. Timmermann, F.-F. Jin, S. McGregor, and H.-L. Ren, 2013: A combination mode of the annual cycle and the El Niño/Southern Oscillation. *Nat. Geosci.*, **6**, 540–544, https://doi.org/10.1038/ngeo1826.

——, F.-F. Jin, A. Timmermann, and S. McGregor, 2015: Combination mode dynamics of the anomalous northwest Pacific anticyclone. *J. Climate*, **28**, 1093–1111, https://doi.org/10.1175/JCLI-D-14-00225.1.

Su, J., R. Zhang, T. Li, X. Rong, J.-S. Kug, and C.-C. Hong, 2010: Causes of the El Niño and La Niña amplitude asymmetry in the equatorial eastern Pacific. *J. Climate*, **23**, 605–617, https://doi.org/10.1175/2009JCLI2894.1.

Suarez, M. J., and P. S. Schopf, 1988: A delayed action oscillator for ENSO. *J. Atmos. Sci.*, **45**, 3283–3287, https://doi.org/10.1175/1520-0469(1988)045<3283:ADAOFE>2.0.CO;2.

Takahashi, K., A. Montecinos, K. Goubanova, and B. Dewitte, 2011: ENSO regimes: Reinterpreting the canonical and Modoki El Niño. *Geophys. Res. Lett.*, **38**, L10704, https://doi.org/10.1029/2011GL047364.

Trenberth, K. E., G. W. Branstator, D. Karoly, A. Kumar, N.-C. Lau, and C. Ropelewski, 1998: Progress during TOGA in understanding and modeling global teleconnections associated with tropical sea surface temperatures. *J. Geophys. Res.*, **103**, 14 291–14 324, https://doi.org/10.1029/97JC01444.

Tziperman, E., L. Stone, M. A. Cane, and H. Jarosh, 1994: El Niño Chaos: Overlapping of resonances between the seasonal cycle and the Pacific ocean–atmosphere oscillator. *Science*, **264**, 72–74, https://doi.org/10.1126/science.264.5155.72.

——, S. E. Zebiak, and M. A. Cane, 1997: Mechanisms of seasonal–ENSO interaction. *J. Atmos. Sci.*, **54**, 61–71, https://doi.org/10.1175/1520-0469(1997)054<0061:MOSEI>2.0.CO;2.

Vimont, D. J., D. S. Battisti, and A. C. Hirst, 2001: Footprinting: A seasonal connection between the tropics and mid-latitudes. *Geophys. Res. Lett.*, **28**, 3923–3926, https://doi.org/10.1029/2001GL013435.

——, ——, and ——, 2003a: The seasonal footprinting mechanism in the CSIRO general circulation models. *J. Climate*, **16**, 2653–2667, https://doi.org/10.1175/1520-0442(2003)016<2653:TSFMIT>2.0.CO;2.

——, J. M. Wallace, and D. S. Battisti, 2003b: The seasonal footprinting mechanism in the Pacific: Implications for ENSO. *J. Climate*, **16**, 2668–2675, https://doi.org/10.1175/1520-0442(2003)016<2668:TSFMIT>2.0.CO;2.

Wang, B., and Q. Zhang, 2002: Pacific–East Asian teleconnection. Part II: How the Philippine Sea anomalous anticyclone is established during El Niño development. *J. Climate*, **15**, 3252–

3265, https://doi.org/10.1175/1520-0442(2002)015<3252:PEATPI>2.0.CO;2.

——, R. Wu, and R. Lukas, 1999: Roles of the western North Pacific wind variation in thermocline adjustment and ENSO phase transition. *J. Meteor. Soc. Japan*, **77** (1), 1–16, https://doi.org/10.2151/jmsj1965.77.1_1.

——, ——, and X. Fu, 2000: Pacific–East Asian teleconnection: How does ENSO affect East Asian climate? *J. Climate*, **13**, 1517–1536, https://doi.org/10.1175/1520-0442(2000)013<1517:PEATHD>2.0.CO;2.

Weisberg, R. H., and C. Wang, 1997: A western Pacific oscillator paradigm for the El Niño–Southern Oscillation. *Geophys. Res. Lett.*, **24**, 779–782, https://doi.org/10.1029/97GL00689.

Wu, B., T. Zhou, and T. Li, 2017a: Atmospheric dynamic and thermodynamic processes driving the western North Pacific anomalous anticyclone during El Niño. Part I: Maintenance mechanisms. *J. Climate*, **30**, 9621–9635, https://doi.org/10.1175/JCLI-D-16-0489.1.

——, ——, and ——, 2017b: Atmospheric dynamic and thermodynamic processes driving the western North Pacific anomalous anticyclone during El Niño. Part II: Formation processes. *J. Climate*, **30**, 9637–9650, https://doi.org/10.1175/JCLI-D-16-0495.1.

Wu, E.-T., 2018: An observational study of anomalous anticyclone in western North Pacific associated with El Niño. M.S. thesis, Dept. of Atmospheric Sciences, National Taiwan University, 55 pp., https://tdr.lib.ntu.edu.tw/handle/123456789/1342.

Wu, X., Y. M. Okumura, and P. N. DiNezio, 2019: What controls the duration of El Niño and La Niña events? *J. Climate*, **32**, 5941–5965, https://doi.org/10.1175/JCLI-D-18-0681.1.

Yu, J.-Y., H.-Y. Kao, and T. Lee, 2010: Subtropics-related interannual sea surface temperature variability in the central equatorial Pacific. *J. Climate*, **23**, 2869–2884, https://doi.org/10.1175/2010JCLI3171.1.

Zhang, L., P. Chang, and L. Ji, 2009: Linking the Pacific meridional mode to ENSO: coupled model analysis. *J. Climate*, **22**, 3488–3505, https://doi.org/10.1175/2008JCLI2473.1.